Fetch-limited, strongly forced wind waves in waters with frazil and grease ice — spectral modelling and satellite observations in an Antarctic coastal polynya

Agnieszka Herman[1], **Katarzyna Bradtke**[2]

[1]Institute of Oceanology, Polish Academy of Sciences, Sopot, Poland
[2]Faculty of Oceanography and Geography, University of Gdansk, Poland

Key Points:

- Spectral wave model tuned to reproduce satellite-derived wave properties (peak period, whitecap fraction) in Terra Nova Bay Polynya.
- Frazil streaks in polynyas modify wind waves by reducing whitecapping and energy input from wind and increasing viscous dissipation.
- Nonlinear wave–wave interactions are crucial in both ice-covered and ice-free areas.

Corresponding author: Agnieszka Herman, agaherman@iopan.pl

Abstract

Sea ice–waves interactions have been widely studied in the marginal ice zone, at relatively low wind speeds and wave frequencies. Here, we focus on very different conditions typical of coastal polynyas: extremely high wind speeds and locally-generated, short, steep waves. We overview available parameterizations of relevant physical processes (nonlinear wave–wave interactions, energy input by wind, whitecapping and ice-related dissipation) and discuss modifications necessary to adjust them to polynya conditions. We use satellite-derived data and spectral modelling to analyze waves in ten polynya events in the Terra Nova Bay, Antarctica. We estimate the wind-input reduction factor over ice in the wave-energy balance equation at 0.56. By calibrating the model to satellite observations we show that exact treatment of quadruplet wave–wave interactions (as opposed to the default Discrete Interaction Approximation) is necessary to fit the model to data, and that the power $n > 4$ in the sea-ice source term $S_{\mathrm{ice}} \sim f^n$ (where f denotes wave frequency) is required to reproduce the observed very strong attenuation in spectral tail in frazil streaks. We use a very-high resolution satellite image of a fragment of one of the polynyas to determine whitecap fraction. We show that there are more than twofold differences in whitecap fraction over ice-free and ice-covered regions, and that the model produces realistic whitecap fractions without any tuning of the whitecapping source term. Finally, we estimate the polynya-area-integrated wind input, energy dissipation due to whitecapping, and whitecap fraction to be on average below 25%, 10% and 30%, respectively, of the corresponding open-water values.

Plain Language Summary

As ocean waves propagate through areas covered with sea ice, they both affect and are affected by the ice. Until recently, wave–ice interactions have been analyzed in the so-called marginal ice zone (MIZ), the external part of sea ice cover neighboring the open ocean. In this work, we study a largely unexplored case of wave–ice interactions that take place in Antarctic coastal polynyas at extremely high wind speeds (often exceeding 100 kph) and low air temperatures (often below $-20°$C). These waves are very different from those in the MIZ and therefore allow us to learn new aspects of the physics of wave growth and dissipation in sea ice. In our study we use numerical wave modeling and satellite data analysis, and seek optimal combinations of model settings to reproduce the observations. For example, we determine a scaling factor that describes how the energy input from wind is reduced over polynyas due to the presence of the ice. We also show that sea ice reduces wave breaking – and that the model is able to reproduce this effect. Taken together, our results contribute not only to a better understanding of polynya dynamics, but also to more reliable modeling of waves in sea ice in general.

1 Introduction

Interactions between sea ice and ocean surface waves have been in recent years extensively studied theoretically, observationally and numerically (Squire, 2018, 2020; Liu et al., 2020; Shen, 2022, and references there). Significance of waves–ice interactions for short-term dynamics of sea ice and the upper ocean, and for longer-term evolution of sea ice cover in (sub)polar regions has been demonstrated in a number of studies (e.g., Roach et al., 2018, 2019; Boutin et al., 2020). The main focus of waves-in-ice research has been on attenuation of ocean waves in sea ice, caused by energy-conserving scattering and/or dissipation within and under the ice. Importantly, the evolution of wave energy spectra in sea ice is usually analyzed on a component-by-component basis, that is, attenuation coefficients are estimated from pairs of observed spectra at two different locations separately for individual frequency bins (e.g., Cheng et al., 2017; Stopa, Sutherland, & Ardhuin, 2018; Kohout et al., 2020; Alberello et al., 2022), disregarding energy exchange between spectral components that is crucial for evolution of ocean surface waves in open

water (e.g., Holthuijsen, 2007). These empirically determined apparent attenuation coefficients are then implemented in spectral wave models (e.g., Collins & Rogers, 2017; Rogers, 2019). Not surprisingly, measurements made in different ice types (frazil, grease ice, pancakes, ice floes, etc.) and ice thickness lead to different estimations of those coefficients (see Rogers, Meylan, & Kohout, 2018, for an overview). A more serious problem with this approach is that the apparent attenuation represents not only sea-ice related scattering and dissipation, but is a net effect of all processes involved, including wind-wave growth, dissipation unrelated to ice, and nonlinear wave–wave interactions. Arguably, disentangling sea ice effects from the net attenuation requires a combination of process-oriented observations and theoretical models capturing the underlying physics. In spite of some recent progress in this respect (see, e.g.., Voermans et al., 2019; Smith & Thomson, 2019a, 2019b; Herman, 2021), the goal of making the spectral wave models in sea ice comparably versatile as they are in open water remains a big challenge.

In attempts to achieve that goal it is important to collect data from a wide range of waves-in-ice conditions. At present, a serious limitation is the fact that our understanding of sea ice–waves interactions is based exclusively on data from and models of the marginal ice zone (MIZ; Dumont, 2022). The focus on the MIZ implies that our observations and modelling efforts are limited to a certain range of conditions typical for this environment. In particular, waves in the MIZ tend to have low u_*/c ratios (where u_* denotes the friction velocity of the wind at the sea surface, and c is wave phase speed; the ratio u_*/c is an inverse of the wave age). In the MIZ typically $u_*/c \ll 0.1$ for wave frequencies at and close to the spectral peak. This means that these waves are weakly forced by wind (Janssen et al., 1989) and, consequently, have low steepness and do not break. As a result, in the spectral energy balance the wind input and wave breaking terms are dominated by terms representing dissipation and scattering in sea ice. It is noteworthy that situations deviating from that picture (e.g., those with negative apparent attenuation indicating dominance of wave growth over dissipation) are often removed from the observations prior to the analysis (e.g., Cheng et al., 2017).

As a step towards broadening the picture and extending wave–ice interactions analyses to a wider range of conditions, we turn our attention towards a setting with features that in many ways are the opposite of the MIZ-typical conditions described above: coastal (or latent heat) polynyas during catabatic wind events (Morales Maqueda et al., 2004). Polynya openings are associated with very high wind speeds, often exceeding 30 $\mathrm{m{\cdot}s^{-1}}$, and advection of very cold and dry continental air masses, resulting in offshore drift of the ice pack and extremely high ocean–atmosphere turbulent heat and moisture fluxes (up to 2000 $\mathrm{W{\cdot}m^{-2}}$; Guest, 2021a, 2021b). All these factors combined lead to strong turbulence and convective, wind- and wave-induced mixing in the ocean mixed layer (OML; Herman et al., 2020), and to intense frazil ice formation (Thompson et al., 2020; Nakata et al., 2021). Crucially for this study, waves in coastal polynyas are young, fetch-limited, strongly forced ($u_*/c > 0.1$), and therefore short and steep, with a strong tendency to break. Over most of polynya area, energy input from the wind dominates over the net dissipation, so that the wave energy grows with offshore distance in spite of increasing ice concentration. Moreover, the sea surface in polynyas is a complex mosaic of open-water areas and patches of young (frazil, grease and shuga) ice forming characteristic elongated streaks (Eicken & Lange, 1989; Ciappa & Pietranera, 2013; Hollands & Dierking, 2016; Thompson et al., 2020). The properties of those streaks in one of the most widely studied Antarctic coastal polynyas, the Terra Nova Bay Polynya (TNBP; Fig. 1), have been recently analyzed by Bradtke and Herman (2023). One of the findings of this previous study was a significant slowdown of the observed wave growth in the analyzed polynya events in comparison to the expected open-water wave growth under given wind conditions, an effect that can be attributed only to wave–ice interactions. Inspired by this finding, in this work we conduct an extensive analysis of wave evolution in a series of TNBP events, based on the results from Bradtke and Herman (2023), an additional satellite data source providing information on wave breaking patterns, and spectral wave modelling.

The overall influence of frazil streaks on waves and, more generally, on the sea surface properties has been described in several earlier studies based on qualitative visual observations (e.g., Ciappa & Pietranera, 2013; Hollands & Dierking, 2016; Ackley et al., 2022). Rapid attenuation of short waves in streaks, attributable to a high bulk viscosity of grease ice, leads to a reduction of surface roughness (and thus wind friction velocity u_*), decrease of the mean wave steepness, and weakening of wave breaking and whitecap generation (Ackley et al., 2022), thus reducing the sea spray generation and the spray-associated component of the ocean–atmosphere turbulent heat flux (Guest, 2021b). The question how to quantify and parameterize these effects and, crucially, how they influence the spatial evolution of the polynya wave field – with feedbacks to sea ice thermodynamics and dynamics – remains to be answered. In this study, we make the first attempt at estimating the role of individual source terms in the wave-energy balance in shaping the polynya wave fields. We use the satellite-derived ice concentration and wave data from Bradtke and Herman (2023), combined with wind fields from a regional weather model, to set up and calibrate a spectral wave model of the TNBP, for ten polynya events from the period 2016–2021. We review the available formulations of the relevant source terms – wind input, deep-water dissipation, quadruplet wave–wave interactions, and attenuation in sea ice – and seek the combination of model settings that best reproduces observations. We also discuss the (numerous) uncertainties and limitations of the available observations and models. In our analysis, we pay particular attention to the influence of frazil streaks on wave breaking. To this end, we adopted an image filtering technique for detection of breakers in very-high resolution (0.5 m) visible satellite images of the sea surface. We then compare the spatial variability of two different, but closely related variables – the satellite-derived surface area fraction covered by breakers, and the simulated wave energy dissipation due to whitecapping – and estimate the reduction of the total (polynya-surface-integrated) energy dissipation due to the presence of sea ice.

2 Data Sources and Processing

2.1 Ice concentration, wave properties and wind data

As mentioned in the introduction, this analysis is based on the data and results of Bradtke and Herman (2023). From the set of satellite images analyzed there, ten have been selected for the present study (Table 1, Supplementary Fig. S1), based on their sufficiently large spatial extent (given the images' resolution of 10 m, no reliable wave information can be obtained from nearshore areas and from relatively small polynyas due to too small wavelength-to-pixel-size ratios). The ten images were obtained with two satellite sensors: OLI (Operational Land Imager) and MSI (Multispectral Instument) on board Landsat-8 and Sentinel-2 satellites, respectively. All details related to image processing and analysis can be found in Bradtke and Herman (2023) and are not repeated here. The data used in this study include, for each polynya, maps of polynya extent, ice concentration A, and peak wavelength L_p (and the corresponding deep-water wave period T_p and frequency $f_p = T_p^{-1}$). As discussed in Bradtke and Herman (2023), the peak wavelength, together with wave direction at the spectral peak (not considered here), are two spectral characteristics that can be robustly determined from visible satellite imagery. Indisputably, the lack of information on wave heights and the shape of the tails of the spectra is a serious limitation. However, as the analysis in the following sections will show, spatial variability of T_p alone provides valuable insight into the properties of the underlying wave field and, crucially, constrains the possible combinations of the adjustable parameters in spectral modelling, thus allowing inferences about individual physical processes at play.

The results of the Antarctic Mesoscale Prediction System (AMPS; Powers et al., 2012, `https://www.earthsystemgrid.org/project/amps.html`) are used as a source of surface atmospheric data. Results from a nested subdomain (the so called Ross Island grid) are used, with resolution of 1.1 km in 2016 and 0.89 km in 2019–2021. For each

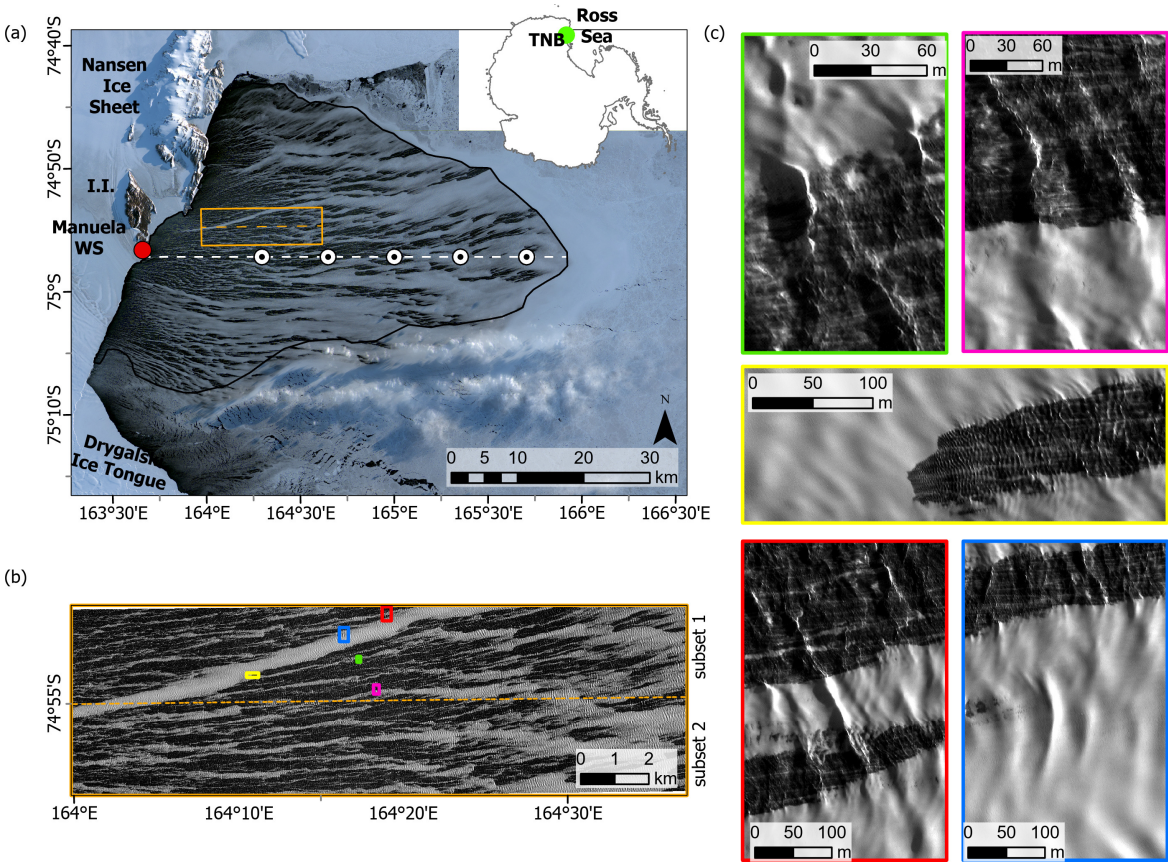

Figure 1. (a) Location of the TNBP and spatial distribution of sea ice on 19 Sep. 2019 on the Sentinel-2 MSI RGB composite (Copernicus Sentinel data 2019); the outline of the polynya and the location of the Manuela weather station on Inexpressible Island (I.I.) are marked with the black polygon and red dot, respectively. The orange rectangle shows extent of the analyzed subsets of WorldView-2 Panchromatic image (imagery © 2019 Maxar Technologies), fragments of which are zoomed in panels (b) and (c). The dashed white line and white dots in (a) show the location of the transect and points at which the results are analyzed in section 4.

Table 1. Summary of polynya events analyzed in this study

Date	Time (UTC)	Sensor	$T_{a,\mathrm{M}}$ (°C)	$U_{w,\mathrm{M}}$ (m·s^{-1})	$\theta_{w,\mathrm{M}}$ (degr)	S_p (km^2)	L_e (km)	L_c (km)
2016-10-05	2120	MSI	−22.5	24.1	260	1043	36.2	63.7
2016-10-06	2050	MSI	−24.6	25.4	262	740	40.8	62.3
2016-10-17	2050	OLI	−21.4	28.4	261	1110	33.8	46.7
2016-10-22	2110	MSI	−22.3	21.3	259	975	28.3	46.8
2016-10-24	2100	OLI	−17.4	28.7	257	1762	53.3	55.2
2019-09-19	2100	MSI	−26.5	33.8	258	1920	56.3	50.0
2019-09-29	2110	OLI	−23.4	32.4	250	1729	45.4	57.9
2020-10-19	2100	OLI	−26.2	23.5	261	674	36.2	46.9
2020-10-26	2100	OLI	−20.6	23.3	266	1648	39.5	65.7
2021-10-07	2130	MSI	−23.2	28.1	272	736	35.5	52.2

$T_{a,\mathrm{M}}$, $U_{w,\mathrm{M}}$, $\theta_{w,\mathrm{M}}$ – air temperature, wind speed and direction, respectively, at the Manuela weather station; S_p – polynya surface area; L_e and L_c – polynya extent in cross-shore and along-shore direction, respectively.

polynya, 9-hour forecasts from 12 UTC valid for 21 UTC were selected, i.e., the time closest to the acquisition time of the satellite scenes (Table 1). The 2-m AMPS wind vectors were recomputed onto the 10-m height with the algorithm based on the Monin–Obukhov similarity theory, as described in Guest (2021b). (Note that the measured wind data from the Manuela weather station in Table 1 are provided for informative purpose only; the wave modelling is based exclusively on the spatially-variable AMPS wind fields.)

2.2 Wave breaking patterns

The only additional source of satellite data used here, but not in Bradtke and Herman (2023), is a very-high resolution panchromatic (PAN) satellite image taken by the WorldView-2 (WV2) satellite (imagery © 2019 Maxar Technologies) showing a fragment of the polynya from 19. Sep. 2019 (see Figs. 1 and 2 for a location and for zoomed fragments). The image was acquired at 21:22 UTC, i.e., 22 minutes after the corresponding MSI image, but considering the stable wind and air temperature forcing on that day it is reasonable to assume that the wave and sea ice conditions were very similar as well. We analyze a fragment of the scene taken by the satellite which covers an area of 18.3×5.5 km^2. We use the standard LV2A product, without atmospheric correction, georeferenced and resampled to a grid of $0.5 \cdot$m (the viewing geometry provides effective resolution of 0.53 m) in UTM zone 58S projection. Due to the small size of the analyzed area and cloudless sky, it can be assumed that the influence of the atmosphere on the image brightness is spatially homogeneous. During the satellite overpass the sea surface was illuminated by the Sun from a direction of 54.1° (azimuth angle) and an elevation angle of 7.7°. With the predominant direction of wave propagation towards the east (see Supplementary Fig. S1), this geometry of illumination causes shadowing of the windward slopes of steep waves. This makes it easier to identify them on a satellite image. However, the limited availability of light makes it impossible to analyze features occurring in shadowed areas of open water.

As can be seen on the WV2 image (Fig. 2), whitecaps strongly contrast with darker water, even if the water reflectance is raised by frazil ice. The lighting conditions make also the very bright crests of steep waves clearly visible against the background of the frazil streaks. Therefore, in order to detect potential breakers in the analyzed image, we were looking for sharp contrast between neighboring pixels by applying a moving-window filter that calculates the sum of differences between a given pixel and the eight nearest pixels in the directions between 225° and 315° (SW to NW). Initially, the panchromatic image was de-noised with an edge-preserving filter. Pixels for which the calculated contrast value was higher than the image average by more than 3 standard deviations (the same threshold for the whole image) were identified as sharply contrasted objects. To limit false alarms, only those objects that met the size criterion (more than 3 pixels connected by sides or corners) and contained bright pixels (the brightness threshold was determined by unsupervised ISODATA classification of the de-noised PAN image) were considered as potential breakers (Fig. 2). In the next step, the surface area of pixels recognized as breakers was used to calculate whitecap fraction W within 200×200 m^2 grid cells snapped to the grid of the wave model (see further section 3.3); and zonal fraction W_X was calculated in vertical zones 200 m wide, oriented perpendicularly to the x_{UTM} axis. Due to differences in spatial patterns of frazil streaks in the upper and lower parts of the PAN image, it was divided into 2 subsets (see Fig. 1b) and zonal statistics were calculated for each of them separately. Finally, ice–water mask derived from WV2 data was used to calculate whitecap fraction W_X separately for ice-free and ice-covered regions, respectively.

Due to the lack of independent observations that could be used to validate our algorithm, its adjustable parameters have been selected in such a way that, first, the outlines of detected breakers (Fig. 2) correspond as close as possible to a visual assessment by a human observer, and second, if any bias in the results is present, it is towards overde-

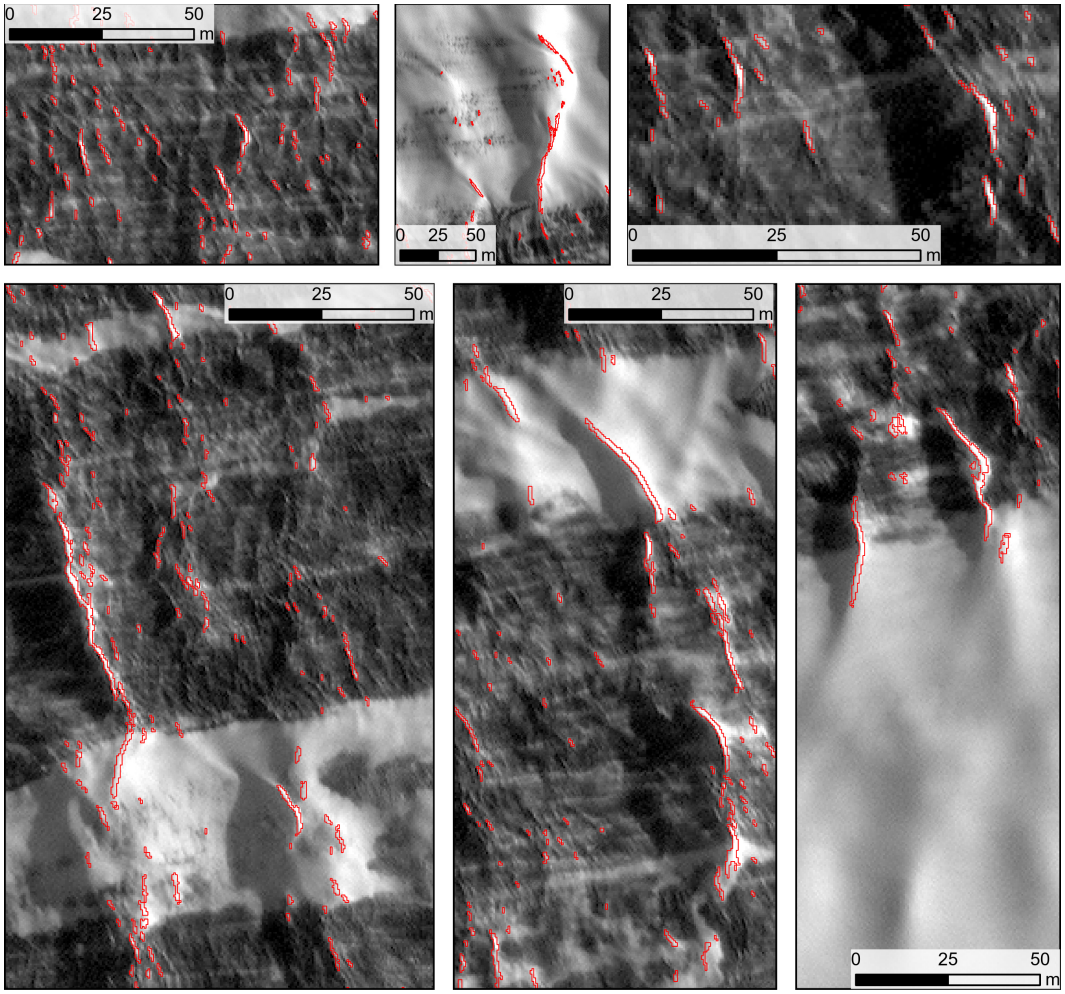

Figure 2. Zoomed fragments of WorldView-2 Panchromatic image (Imagery ©2019 Maxar Technologies) showing variability in pixel brightness due to the presence of frazil ice, waves and effects of their breaking. Outlines of detected breakers are marked in red.

tection in ice and underdetection in water rather than *vice versa*. Thus, in spite of unavoidable uncertainties, the differences between ice-covered and ice-free regions can be treated as reliable and under- rather than overestimated.

Image processing and visualization was performed with the Trimble eCognition Developer and ESRI ArcGIS Pro software.

3 Spectral Wave Modeling

3.1 Definitions and assumptions

Let us consider a stationary wave field described by spatially variable wave energy spectra $E(\mathbf{x}, f, \theta)$, where $\mathbf{x}$ is location in horizontal space, and f, θ are wave frequency and propagation direction, respectively. Let us further assume that the waves are forced by time-independent wind with 10-m speed $u_{10}(\mathbf{x})$ and direction $\theta_{\mathrm{w}}(\mathbf{x})$, and that the water depth is large, so that refraction, bottom friction and other processes related to wave–

bottom interactions can be omitted. The wind-induced, tidal and other currents are omitted as well. Finally, let the sea ice concentration be described by $A(\mathbf{x})$.

Under these assumptions, the wave energy conservation equation (e.g., Holthuijsen, 2007) reduces to:

$$\mathbf{c}_g \cdot \nabla E = [1 - A + a_{\mathrm{in}} A] S_{\mathrm{in}} + S_{\mathrm{ds}} + S_{\mathrm{nl}} + A S_{\mathrm{ice}}, \tag{1}$$

where $\mathbf{c}_g = c_g[\cos\theta, \sin\theta]$, $c_g = \mathrm{d}\sigma/\mathrm{d}k$ is the group velocity, and the angular frequency $\sigma = 2\pi f$ and wave number k fulfill the deep-water dispersion relation $\sigma^2 = gk$, with g gravitational acceleration. No changes of the dispersion relation due to the presence of frazil/grease ice are considered here – an assumption consistent with that of a low thickness and low Reynolds number of frazil/grease ice in streaks (e.g., Collins et al., 2017, note that observations and models of wave dispersion in frazil ice referred to in this and similar papers are limited to frazil/pancakes mixtures typical for freezing conditions in the MIZ – ice type that can be found in the outermost regions of polynyas, but not in their central parts of interest here). The source terms on the right-hand side of (1) describe energy generation by wind S_{in}, deep-water dissipation S_{ds}, quadruplet wave–wave interactions S_{nl}, and attenuation by sea ice S_{ice}. As can be seen in (1), S_{ice} is scaled with ice concentration A. The coefficient $a_{\mathrm{in}} \in [0, 1]$ allows for analogous scaling of S_{in}: the wind input is unaffected by ice if $a_{\mathrm{in}} = 1$ and it equals zero over ice if $a_{\mathrm{in}} = 0$. The two remaining source terms, S_{ds}, S_{nl}, are unaffected by the presence of the ice. Justification for this treatment of source terms is provided below.

3.2 Overview of source terms formulations

In most spectral wave models (e.g., SWAN, WaveWatchIII, or WAM), several different formulations of each source term in (1) are implemented. Their optimal choice depends on a particular application (domain size, water depth, expected u_*/c ratios, presence of swell, etc.). Reviewing those formulations is out of the scope of this paper. Instead, we concentrate here on selected parameterizations suitable for polynya conditions, with focus on those available in SWAN (Simulating WAves Nearshore; Booij et al., 1999), which is the model used in our simulations. Whenever several choices seem adequate, the more widely used ones (or, preferably, default) are selected.

3.2.1 S_{nl}

Starting with the S_{nl} term, it is important to recall that the nonlinear wave–wave interactions are inherently related to the dispersion relation of waves or, more precisely, to the existence of certain combinations of wavenumber vectors and wave frequencies among the components of the wave energy spectra (resonance conditions; see, e.g., Holthuijsen, 2007). Therefore, as long as the assumptions made in section 3.1 hold (large water depth and validity of the open-water dispersion relation in frazil streaks), it is reasonable to assume that the quadruplet wave–wave interactions remain "active" and can be computed in the same way in ice-covered and ice-free areas (it should be noted, however, that in different ice types different types of nonlinear interactions may occur, e.g. triads in fields of large floes in which hydroelastic effects are significant, see, e.g., Deike et al., 2017).

In SWAN and other spectral wave models, the DIA (discrete interaction approximation) by Hasselmann et al. (1985) is the default way of computing S_{nl}. Out of the very large number of quadruplet combinations in a given energy spectrum, DIA considers only two quadruplets for each spectral component (see SWAN Team, 2022, for details of DIA and its implementation in SWAN). Without making premature references to our model setup and simulations, we remark here that in spite of many attempts, we were unable to calibrate SWAN to the data when using DIA: the simulated wave periods were strongly biased in a way that could not be reduced by any reasonable combi-

nation of tunable coefficients. Replacing the DIA with the near-exact method (Van Vledder, 2006) removed the problems, suggesting that a careful treatment of quadruplet interactions is crucial for reproducing wave growth in polynyas (and in similar settings) with spectral wave models. This finding is not surprising if one considers the crucial role of nonlinear wave–wave interactions in modifying waves propagating through oil spills. Although energy dissipation within the oil layer is limited to very short waves, with frequencies well over 1 Hz (with particularly strong attenuation in the range 3.5–6.8 Hz due to Marangoni resonance), transfer of energy from lower frequencies to that highly dissipative frequency range by quadruplets leads to a very effective dissipation mechanism, attenuating waves with frequencies as low as 0.7 Hz (Alpers & Hühnerfuss, 1989; Benetazzo et al., 2019). How relevant similar combinations of processes are for sea ice remains to be studied. Notably, the importance of nonlinear interactions (combined with wind input) in reproducing the observed apparent attenuation rates of high-amplitude waves in the MIZ under storm conditions has been shown by Li et al. (2015).

3.2.2 S_{in} *and* S_{ds}

For S_{in} and S_{ds} – the two source terms that are very closely related in spectral wave models (Holthuijsen, 2007) – the formulation of Van der Westhuijsen et al. (2007) is selected. It combines wind input of Yan (1987) with nonlinear saturation-based whitecapping based on Alves and Banner (2003) and dissipation due to non-breaking waves based on Komen et al. (1984). Contrary to earlier models of whitecapping, which computed breaking probability from spectral-mean wave steepness (Komen et al., 1984), the formulation of Alves and Banner (2003) and the modified version of Van der Westhuijsen et al. (2007) used in SWAN make use of the observed links between wave breaking and wave groups. Accordingly, the so-called spectral saturation $B(k)$ – a measure of wave steepness – is computed from directionally-integrated spectrum $\bar{E}(f) \equiv \int_{\theta=0}^{2\pi} E(f,\theta)\mathrm{d}\theta$ within narrow frequency bands. Thus, dissipation is local in the wavenumber space. This is particularly relevant for the present case: it allows for breaking of short, steep, fast-growing waves in open-water patches between frazil streaks, even if the longer waves at the peak of the spectrum have milder slopes, so that the spectral-average wave steepness does not exceed the critical value. The older algorithms fail to reproduce this case of breaking limited to the narrow frequency range of the spectrum. Importantly as well, although S_{ds} is routinely referred to as the 'whitecapping source term', it is in fact supposed to represent all (largely unknown) deep-water dissipation mechanisms, including turbulence. S_{ds} is thus computed as a weighted sum of two contributions, whitecapping S_{wc} and dissipation unrelated to wave breaking S_{nbr}:

$$S_{\mathrm{ds}} = f_{\mathrm{br}} S_{\mathrm{wc}} + (1 - f_{\mathrm{br}}) S_{\mathrm{nbr}}, \tag{2}$$

where $f_{\mathrm{br}} \in [0, 1]$. For S_{wc} we have:

$$S_{\mathrm{wc}} = -C_{\mathrm{ds}} \left[\frac{B(k)}{B_{\mathrm{r}}}\right]^{p/2} (gk)^{1/2} E(f,\theta), \tag{3}$$

where the saturation $B(k) = c_g k^3 \bar{E}(f)$, and C_{ds}, B_{r} and p are tuning coefficients (see SWAN Team, 2022, for their treatment in SWAN). Details of calculation of S_{nbr} and f_{br} can be found in the SWAN documentation. Crucially, in strongly forced, short waves analyzed here, $f_{\mathrm{br}} \simeq 1$ over the whole energy-carrying wave frequency range (f between, approximately, 0.13 and 0.6 Hz), i.e., both around the peak and in the tail of the spectrum (0.13 Hz is the lowest peak frequency found in satellite images analyzed in this study). Thus, $S_{\mathrm{ds}} \simeq S_{\mathrm{wc}}$. Under different conditions, when $f_{\mathrm{br}} < 1$ and the contribution of S_{nbr} to S_{ds} is substantial, it might be suitable to multiply S_{nbr} by ice concentration A in order to turn off S_{nbr} over ice (reflecting the fact that frazil and grease ice suppresses turbulence due to its large viscosity). In our simulations it did not produce any noticeable differences in the results.

In general, very little is known about wave breaking in frazil and grease ice. As discussed further in section 4.2 and as can be seen in Figs. 1 and 2, long waves do occasionally break within ice streaks in TNBP, although much less frequently than in the surrounding open water. As in the case of S_{nl}, we may seek analogies with oil slicks, for which available observations suggest that the oil's high (and legendary) effectiveness in suppressing wave breaking is a secondary effect of other processes rather than a direct mechanical response of the waves to the oil presence (e.g., Cox et al., 2017). For spectral modelling it means that – provided other source terms are properly computed – the effect of reduced whitecap dissipation in ice-covered areas should be obtained as a modelling result in spite of S_{wc} being computed in the same way everywhere (note that this is the default setting in SWAN).

As for the wind input term S_{in}, its general form is:

$$S_{\mathrm{in}} = \beta_{\mathrm{in}} E, \quad \text{where} \quad \beta_{\mathrm{in}} \equiv \beta_{\mathrm{in}}(u_*/c, \theta_{\mathrm{rel}}) \tag{4}$$

and where θ_{rel} is the angle between wind direction and propagation direction of the given spectral component. In the model of Yan (1987):

$$\beta_{\mathrm{in}} = \max\left\{\left[a_1\left(\frac{u_*}{c}\right)^2 + a_2\frac{u_*}{c} + a_3\right]\cos\theta_{\mathrm{rel}} + a_4, 0\right\}. \tag{5}$$

The coefficients used in SWAN (recalibrated from the original ones by Van der Westhuijsen et al., 2007) are: $a_1 = 4.0\cdot10^{-2}$, $a_2 = 5.52\cdot10^{-3}$, $a_3 = 5.2\cdot10^{-5}$, $a_4 = -3.02\cdot10^{-4}$. An important advantage of this model is that, contrary to the earlier ones formulated for low wind speeds, it is suitable for strongly forced waves as well. As will be shown below, in polynyas this condition is fulfilled over most of both geographic and spectral space (i.e., the majority of polynya surface area, and energy-carrying wave frequency range), with an exception of the longest waves at the downwind end of the polynya.

For a given 10-m wind speed u_{10}, change in S_{in} due to the presence of sea ice may result from three factors: (i) change of the form of the β_{in} function (5); (ii) change of the wave phase speed c due to a modified dispersion relation in ice; and (iii) change of u_* due to a modified roughness of the surface. If we assume that expression (5) remains valid – to the best of our knowledge there are no data available that could be used to verify this assumption – and if we keep the assumption made earlier about the dispersion relation in polynyas, the only factor that remains is the surface drag. (Note that the influnce of the dispersion relation in sea ice on wind wave growth has been analyzed by Zhao & Zhang, 2020)

The relationship between u_* and u_{10} is $u_*^2 = C_{\mathrm{D}}u_{10}^2$, where C_{D} is the 10-m drag coefficient. In spectral wave models, $C_{\mathrm{D}} = C_{\mathrm{Dn}}$, i.e. it represents the neutral drag coefficient and it is a function of u_{10} only. The default $C_{\mathrm{Dn}}(u_{10})$ relationship used in SWAN is by Zijlema et al. (2012), which reproduces the observed drop of surface drag at very high wind speeds (Janssen & Bidlot, 2023):

$$C_{\mathrm{Dn}} = \left(0.55 + 2.97\tilde{u} - 1.49\tilde{u}^2\right)\cdot10^{-3}, \quad \text{where} \quad \tilde{u} = u_{10}/u_{\mathrm{ref}} \tag{6}$$

and $u_{\mathrm{ref}} = 31.5$ m·s^{-1} is a reference wind speed at which C_{Dn} reaches maximum. This formulation disregards possible spatial variability in surface properties, as well as effects of atmospheric stability – both factors which very likely are important in polynyas, with complicated spatial patterns of frazil–open water patches, and at air temperature T_{a} often 20–30°C lower than the sea surface temperature $T_{\mathrm{s}} \simeq -1.7$°C (see Table 2.1 for T_{a} during the analyzed events).

The wind drag over open ocean has been analyzed for many years under a wide range of wind and sea state conditions. Over vast areas of the oceans, especially far from the coasts and frontal zones, the assumption $C_{\mathrm{D}} \simeq C_{\mathrm{Dn}}$ is justified, because the air–sea temperature differences tend to be small. At very low air temperatures, however, the neg-

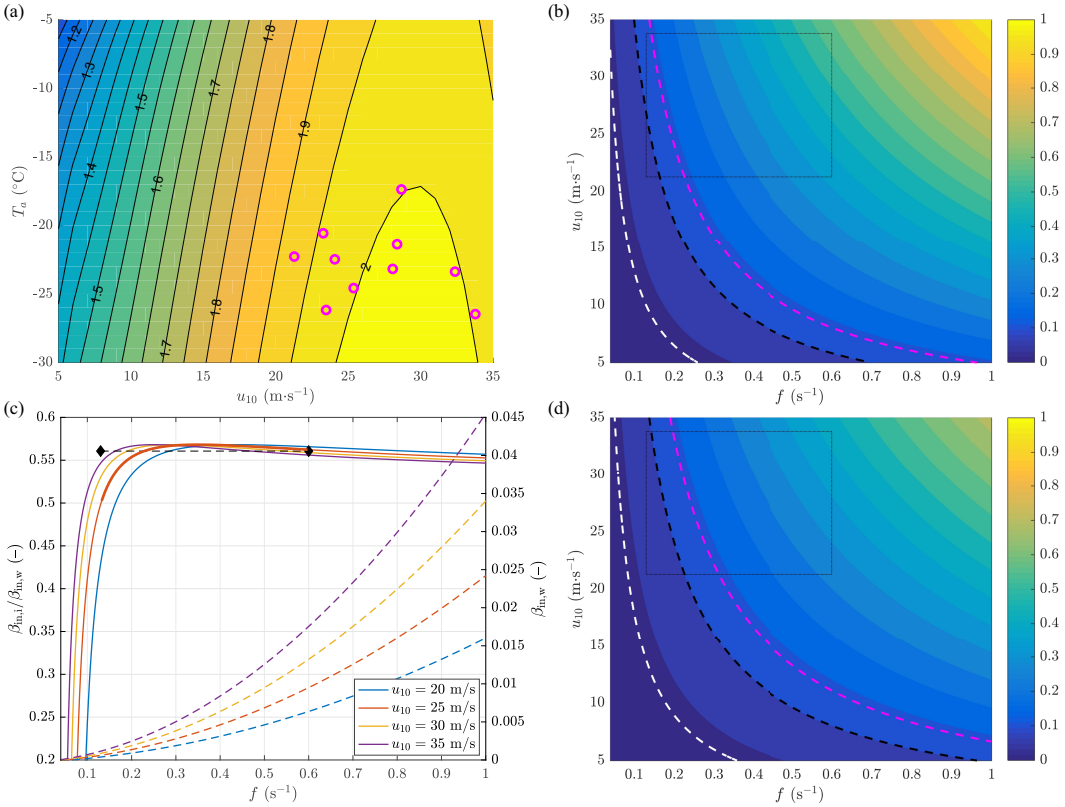

Figure 3. Surface drag and wind input over open water and sea ice. In (a), colors show the open-water surface drag coefficient $C_D(u_{10}, T_a)$ (in 10^3); magenta symbols mark the ten (u_{10}, T_a) combinations in the analyzed TNBP events (Table 1). In (b), colors show the open-water u_*/c ratio (–) in function of wave frequency f and wind speed u_{10}. The dashed contours mark: the value of $\beta_{\mathrm{in,w}} = 0$ (white), $u_*/c = 0.1$ (black) and $u_*/c = a_2/a_1 \simeq 0.14$ (magenta). The dotted rectangle marks the approximate boundary of a region relevant for polynyas (see text for details). In (c), the ratio $\beta_{\mathrm{in,i}}/\beta_{\mathrm{in,w}}$ is shown for four selected values of wind speed (continuous lines; left axis), together with the corresponding curves for $\beta_{\mathrm{in,w}}$ (dashed lines; right axis). The black line with diamonds shows the mean ratio $\beta_{\mathrm{in,i}}/\beta_{\mathrm{in,w}}$ at $u_{10} = 25$ m·s^{-1} within the frequency range $f \in [0.13, 0.6]$ Hz (thick red line). Panel (d) is analogous to (b), but for sea ice instead of open water. Note that all results in (a)–(d) are for $\theta_{\mathrm{rel}} = 0$; they change very little for $|\theta_{\mathrm{rel}}| < 30°$.

ative vertical stability of the lower atmosphere leads to a stronger ocean–atmosphere coupling and increased drag at the surface (an effect that, over polynyas, is partially reduced by very high wind speeds). For C_{Dn} given by (6), $C_{\mathrm{D}}(u_{10}, T_{\mathrm{a}})$ can be determined using the Monin–Obukhov stability theory. The result is shown in Fig. 3a, together with the combinations of u_{10} and T_{a} in the analyzed polynya events (magenta symbols). As they all cluster at the plateau of relatively constant values of C_{D}, in the rest of this analysis we set, for the sake of simplicity, the open-water drag to $C_{\mathrm{Dw}} = 2 \cdot 10^{-3}$.

Studies on the surface drag over an ice-covered ocean concentrate mainly on the Arctic ice pack and the MIZ, i.e., conditions where the surface morphology and the associated form drag play an important role (e.g., Garbrecht et al., 2002; Lüpkes & Birnbaum, 2005; Lüpkes et al., 2012; Mchedlishvili et al., 2023). Observations for frazil and grease ice are rare and limited to low-wind and mildly-sloped wave conditions (see Guest, 2021b, and references there). For frazil and grease ice, drag coefficients between $0.7{\cdot}10^{-3}$

and $1.3{\cdot}10^{-3}$ have been reported. No formula relating wind speed to surface drag, analogous to (6) and valid for frazil/grease sea ice has been proposed so far. In polynyas, the sea surface in ice-covered areas is characterized by the presence of long waves (with length and amplitude similar to those in the surrounding open water) and absence of high-frequency waves (Fig. 1). It is an open question how these unique surface properties – very smooth at length scales of centimeters to meters, undulating at length scales of tens of meters – modify the bulk drag coefficient. Aware of uncertainties behind this assumption, we select the middle value from the range reported above ($1{\cdot}10^{-3}$), increase it by 5% to account for stability effects analogous to those in open water (Fig. 3a), and arrive at the value $C_{\mathrm{Di}} = 1.05 \cdot 10^{-3}$ for ice-covered parts of the polynyas.

With these C_{Dw} and C_{Di}, the ratio u_*/c can be computed for a range of (f, u_{10}) combinations over open water and ice (Fig. 3b,d). When the wind speed is low and the waves are long (MIZ-typical conditions), u_*/c is small and, consequently, in equation (5), the second term in square brackets is larger than the first one (regions to the left of the dashed magenta lines in Fig. 3b,d). Thus, β_{in} is approximately linearly proportional to u_*/c and its values are very low (they equal zero to the left of the dashed white lines in Fig. 3b,d). Conversely, for short waves and high wind speeds, β_{in} is large and proportional to $(u_*/c)^2$. Crucially, over both ice and open water, most of the combinations of f and u_{10} relevant for polynyas lie in the strongly-forced regime (dotted rectangles in Fig. 3b,d). For wind speeds between, say, 20 and 35 $\mathrm{m{\cdot}s^{-1}}$, the ratio $\beta_{\mathrm{in,i}}/\beta_{\mathrm{in,w}}$ decreases slowly with f (it approaches $C_{\mathrm{Di}}/C_{\mathrm{Dw}}$ as $f \to \infty$), but it remains fairly constant for wave frequencies $f > 0.2$ Hz (Fig. 3c). It drops rapidly to very low values as f drops below 0.2 Hz, but for those long waves β_{in} itself is very small (dashed lines in Fig. 3c) – if these waves grow, its due to nonlinear wave–wave interactions and not due to direct energy input from the wind. Therefore, for the sake of simplicity, we set a_{in} in (1) to a constant value, equal to the mean $\beta_{\mathrm{in,i}}/\beta_{\mathrm{in,w}}$ over frequency range $f \in [0.13, 0.6]$ Hz at wind speed $u_{10} = 25$ $\mathrm{m{\cdot}s^{-1}}$ (a typical value for our set of TNBP events). Thus, $a_{\mathrm{in}} = 0.56$ in all our simulations, as marked with the black line in Fig. 3c.

By drawing an analogy to oil slicks once again, we notice that the observed ratios of u_* over slicks to that over open water are close to 0.8 (e.g., Alpers & Hühnerfuss, 1989), leading to the ratios $\beta_{\mathrm{in,i}}/\beta_{\mathrm{in,w}}$ of 0.66–0.67, higher than but comparable to our estimate.

3.2.3 S_{ice}

Finally, for the ice dissipation term S_{ice} in (1), an empirical expression used in both SWAN and WaveWatchIII wave models (Collins & Rogers, 2017; Rogers, 2019) has the form of a sum:

$$S_{\mathrm{ice}} = \alpha_{\mathrm{ice}} E = \sum_{n=0}^{n_{\mathrm{m}}} \alpha_{\mathrm{ice},n} f^n E, \tag{7}$$

where $\alpha_{\mathrm{ice},n}$ for $n = 1, \ldots, n_{\mathrm{m}}$ are coefficients that can be tuned to a particular situation or set to values from one of the published studies (see, e.g., Rogers, Meylan, & Kohout, 2018; Rogers, Posey, et al., 2018, for an overview of available formulae). The default settings in SWAN are from Meylan et al. (2014), with $\alpha_{\mathrm{ice},2} = 1.06{\cdot}10^{-3}$ $\mathrm{s^2m^{-1}}$, $\alpha_{\mathrm{ice},4} = 2.3{\cdot}10^{-2}$ $\mathrm{s^4m^{-1}}$ and the remaining $\alpha_{\mathrm{ice},n}$ equal to zero. With this set of coefficients, the energy attenuation in ice gradually changes slope from f^2 for long waves to f^4 in the tail of the spectrum. Several subsequent studies use this form of S_{ice} with retuned $\alpha_{\mathrm{ice},2}$ and $\alpha_{\mathrm{ice},4}$ (e.g., Rogers, Meylan, & Kohout, 2018; Rogers et al., 2021). Generally, their values in frazil and grease ice are even a few times lower than in pancakes and ice floes. Some observations provide evidence for f^5 or f^6 in the spectral tail (Rogers et al., 2021, and references there), leading to a different combination of zero and non-zero coefficients in (7).

Notably, S_{ice} in (7), being purely empirical, does not differentiate between various physical energy dissipation mechanisms that are relevant in different ice types. The change

of slope of $\alpha_{\mathrm{ice}}(f)$ from low to high wave frequency, described above, is often attributed to different (combinations of) physical attenuation mechanisms dominating in the long-wave and short-wave parts of the spectrum. In frazil and grease ice analyzed here, however, it seems reasonable to assume that viscous dissipation is the only relevant process and that, at least within the relatively narrow frequency range carrying most energy, a single exponent n can be used for all f.

Additional formulations of S_{ice} with dependence on ice thickness have been proposed and are implemented in SWAN. They are not considered here. As this study concentrates on the active-frazil parts of polynyas, i.e., before the ice consolidates into a relatively compact ice cover, no significant effects of ice thickness are expected. Analogously, we do not consider here a source term describing wave scattering in sea ice, as this process is not relevant in frazil and grease ice.

3.3 Model setup and simulations

The simulations in this analysis are performed with SWAN version 41.45 (`http://www.swan.tudelft.nl`). In accordance with the assumptions formulated in section 3.1, several simplifications are made in the model setup. A rectangular model domain with 200 m spatial resolution is used, with realistic coastlines, but a constant water depth of 500 m. For each polynya, two sea ice maps have been prepared, one with ice concentration within the polynya $A = 0$ (for reference, open-water model runs; see below), and one with ice concentration obtained by averaging the values of A determined in Bradtke and Herman (2023) within each 200×200 m^2 grid cell of the model. In both cases, the ice pack surrounding the polynya has ice concentration $A = 1$. The model is run in a stationary mode and forced with wind fields from AMPS (section 2). No currents are taken into account. In spectral space, directional resolution of 10° and 52 frequency bins logarithmically spaced between 0.05 and 1.576 Hz are used. Thus, the maximum frequency is close to six times the highest expected peak frequency ($\sim$0.25 Hz), and the frequency increment factor equals 1.07, as recommended for simulations with the near-exact quadruplet wave–wave interaction algorithm (SWAN Team, 2022).

In the simulations, several combinations of a_{in}, and α_{ice} are considered, as listed in Table 2. Setup S0, with $a_{\mathrm{in}} = 1$ and $\alpha_{\mathrm{ice}} = 0$ provides a reference, open-water test case. In setup S1, wind input over sea ice is turned off ($a_{\mathrm{in}} = 0$) and this is the only effect ice has on waves ($S_{\mathrm{ice}} = 0$). In setup group S2, $a_{\mathrm{in}} = 0.56$, as determined in section 3.2. S2_0 is analogous to S1. In S2_f24 (M14) the default SWAN settings for S_{ice} are used, based on Meylan et al. (2014). In the remaining four setups the sea ice source term is fitted to observations by running the model several times with different combinations of coefficients and selecting the version that results in the best agreement between satellite-derived and simulated peak wave periods. Among many possible criteria of 'the best' agreement, the mean bias has been selected, as this is the main deficiency of setup S0 that we aim at removing. Thus, the optimization is stopped when the relative bias, defined as the average ratio $(T_{p,\mathrm{obs}}-T_{p,\mathrm{mod}})/T_{p,\mathrm{obs}}$, does not exceed 1% (Table 2). The resulting $\alpha_{\mathrm{ice}}(f)$ are shown in Fig. 4.

Obviously, many more combinations of non-zero $\alpha_{\mathrm{ice},n}$ than those considered here could be tested, including those that are predicted by various theoretical models of viscous and viscoelastic dissipation in sea ice (Meylan et al., 2018). However, as we have no means to extract quantitative information on spectral tails from the available satellite imagery, insight gained from additional simulations would be rather limited. As we demonstrate in the next section, setups S2_f4, S2_f5 and S2_f6 are sufficient to illustrate the sensitivity of the model to ice-related dissipation at high wave frequencies and to formulate some important conclusions regarding frequency dependence of S_{ice} in polynyas.

Table 2. Summary of SWAN simulations: sea-ice related model parameters and model performance

	Model parameters		Statistics of T_p			
Setup ID	a_{in}	$\alpha_{\mathrm{ice},n}$	c.c.	bias	rel. bias	s.d.d.
S0	1	0 for all n	0.87	1.15 s	0.19	0.49 s
S1	0	0 for all n	0.80	−0.06 s	−0.01	0.39 s
S2_0	0.56	0 for all n	0.85	0.66 s	0.11	0.42 s
S2_f24 (M14)	0.56	$\alpha_{\mathrm{ice},2} = 1.06 \cdot 10^{-3}$, $\alpha_{\mathrm{ice},4} = 0.230 \cdot 10^{-1}$	0.84	0.34 s	0.06	0.40 s
S2_f24 (fitted)	0.56	$\alpha_{\mathrm{ice},2} = 0.53 \cdot 10^{-3}$, $\alpha_{\mathrm{ice},4} = 1.035 \cdot 10^{-1}$	0.80	−0.02 s	−0.003	0.43 s
S2_f4 (fitted)	0.56	$\alpha_{\mathrm{ice},4} = 1.2 \cdot 10^{-1}$	0.87	0.07 s	0.01	0.37 s
S2_f5 (fitted)	0.56	$\alpha_{\mathrm{ice},5} = 0.66$	0.86	0.04 s	0.01	0.40 s
S2_f6 (fitted)	0.56	$\alpha_{\mathrm{ice},6} = 3.2$	0.83	0.05 s	0.01	0.45 s

c.c. – correlation coefficient, s.d.d. – standard deviation of differences

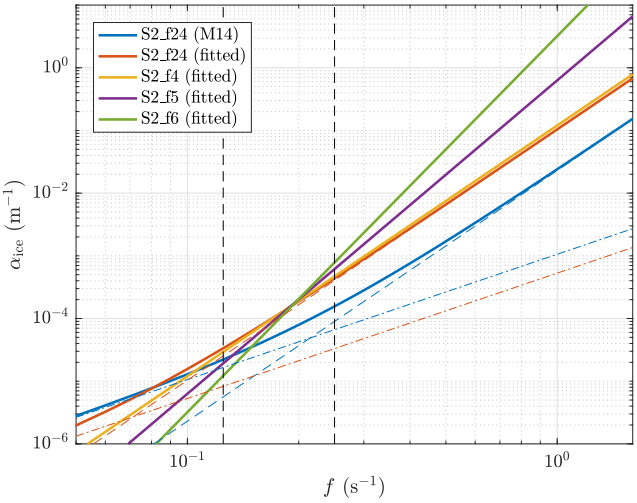

Figure 4. The five $\alpha_{\mathrm{ice}}(f)$ curves considered in model version S2. Blue and red thin dashed lines show the components of the two versions of S2_f24 (M14 and fitted), and the black vertical lines mark the range of wave frequencies corresponding to the observed peak periods.

4 Results

In the following, we first compare the performance of the tested model setups (Table 2) in terms of their ability to reproduce the observed patterns of peak periods T_p in all ten polynya events. Subsequently, we perform a detailed analysis of the satellite observations and modelling results for the polynya from 19. Sep. 2019. It is selected for this purpose for two reasons. First, due to its very large size, it covers the whole range of observed wave periods in the analyzed dataset. Second, it is the only image for which the (nearly) simultaneous wave breaking patterns could be obtained from the WV2 image, as described in section 2.2. The whitecap fraction W and energy dissipation S_{wc} within the WV2 scene and over the whole polynya are discussed in section 4.3. Finally, in section 4.4, we return to the whole dataset of 10 polynyas and analyze global (polynya-surface averaged) statistics of individual source terms.

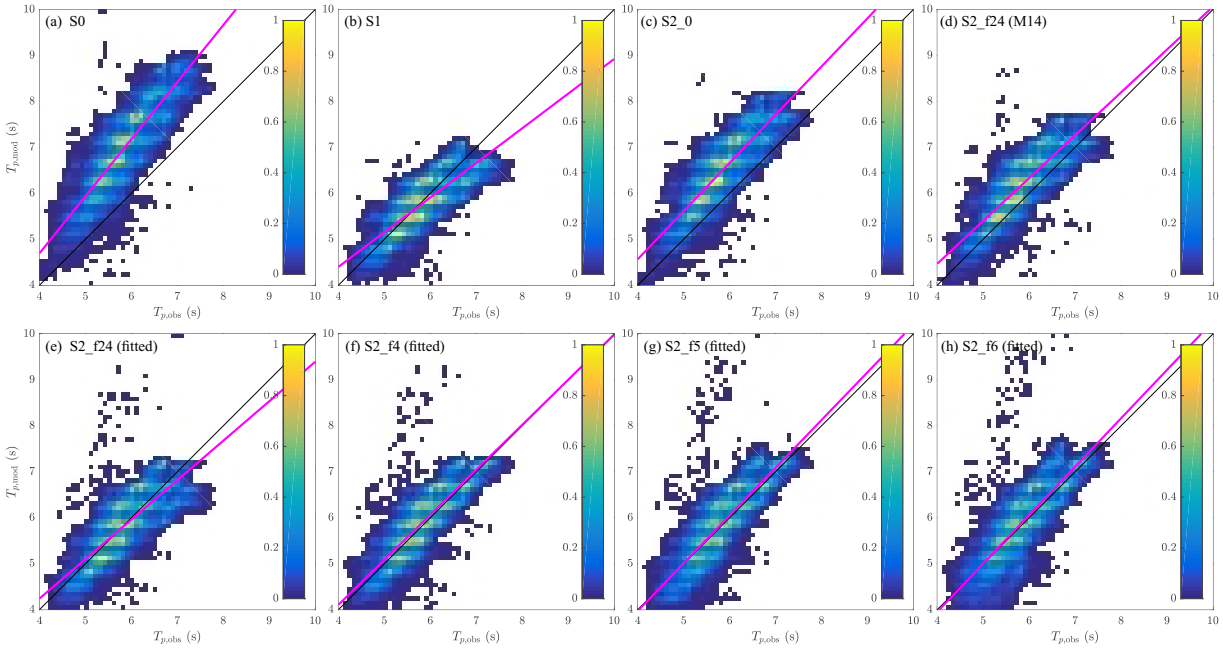

Figure 5. Scatterplots of observed and modelled peak periods, $T_{p,\mathrm{obs}}$ and $T_{p,\mathrm{mod}}$, from the simulations listed in Table 2. The color scale shows values in percent of the total number of data points (i.e., all values in each plot sum up to 100), and magenta lines show the linear regression to the data.

4.1 Performance of the tested model setups

For the purpose of model–observations comparison, the satellite-derived maps of T_p from the 10 polynyas are averaged within the meshes of the SWAN grid, resulting in a dataset of over $2.3{\cdot}10^5$ values. The observed peak periods have values between 4 and 8 s, with the mean and median equal to 5.87 s and 5.81 s, respectively.

As expected from the results of a simple one-dimensional (1D) model in Bradtke and Herman (2023), setup S0 significantly overestimates the wave periods – on average by 1.15 s or close to 20% (Table 2 and Fig. 5a). This effect occurs in spite of the well documented tendency of SWAN and other spectral models to underestimate wave periods (see, e.g., Rogers et al., 2003). Moreover, the AMPS wind speeds used as model input generally tend to be slightly lower than the wind speeds measured at the Manuela station, i.e., if there is a bias in the model forcing, it is towards too weak rather than too strong winds. Thus, as already concluded in Bradtke and Herman (2023), sea ice is the only likely factor responsible for the discrepancy between the observed wave periods and those expected in open water.

Not surprisingly, the bias is reduced in setup S1, with $a_{\mathrm{in}} = 0$, even though no energy dissipation in sea ice is assumed. In fact, the mean bias in S1 is close to zero, and the standard deviation of differences is reduced relative to S0. However, these improvements are achieved at the cost of lowered correlation coefficients; moreover, the model clearly underestimates the large wave periods (Fig. 5b), i.e., the wave growth is inhibited in downwind parts of polynyas with high ice concentration. Obviously, the assumption behind S1 that the influence of frazil streaks is strong enough to completely shut down the wind input, but at the same time that the ice has no direct influence on waves through dissipation, seems unrealistic. However, adding to S1 any $\alpha_{\mathrm{ice}} > 0$ would lead to an even worse model performance and to a negative bias. Hence, the lack of wind in-

put over ice-covered areas is an unlikely explanation for the observations and, accordingly, 'deactivation' of S_{in} over ice is not a good choice.

As can be seen in Table 2, setting a_{in} to 0.56 as in S2_0 reduces approximately half of the mean bias of S0 (Fig. 5c), with a still further reduction in setup S2_f24 (M14), i.e., when the default S_{ice} SWAN setting is used (Fig. 5d). The performance can be improved further by fitting $\alpha_{\mathrm{ice},2}$ and $\alpha_{\mathrm{ice},4}$. However, the fitted value of $\alpha_{\mathrm{ice},2}$ is twice as low as in the corresponding setup with M14, and $\alpha_{\mathrm{ice},4}$ is over four times higher, meaning that the fitted α_{ice} is dominated by the f^4 term: the change of slope towards f^2 takes place at frequencies well below 0.1 Hz, i.e., outside of the range of wave frequencies found in our dataset (compare blue and red curves in Fig. 4). Indeed, dropping the $\alpha_{\mathrm{ice},2}$ term as in S2_f4 results in the fitted value of $\alpha_{\mathrm{ice},4}$ very close to that in S2_f24 (Table 2). Moreover, although setup S2_f4 has only one fitted coefficient as opposed to two in S2_f24, it gives the best global statistics not only in terms of the mean bias, but also the correlation coefficient and standard deviation of differences – and it performs well in the whole range of the observed values of T_p (Fig. 5f). Therefore, the simpler version S2_f4 is preferred over S2_f24.

Finally, the last two tested setups are S2_f5 and S2_f6, which, as expected, leads to a stronger (weaker) attenuation of the lowest (highest) wave periods (Fig. 5f–h). With increasing power n the scatter gets slightly higher and the correlation coefficient lower (Table 2), but, arguably, the differences between the global statistical measures of setups S2_f4, S2_f5 and S2_f6 are rather subtle. This is not surprising as the analysis so far is limited to the peak periods, i.e., the frequency range in which the strength of dissipation in S2_f4, S2_f5 and S2_f6 is very similar (Fig. 4). The differences between these setups can be expected to be more substantial in the tails of the wave energy spectra. Unfortunately, as stated earlier, we cannot perform any quantitative comparison between the observed and modelled spectral tails. However, as we will see in the next section, large qualitative differences between the results of S2_f4, S2_f5 and S2_f6 allow for some (careful) conclusions.

4.2 The polynya from 19. Sep. 2019

The polynya from 19. Sep. 2019 (Fig. 1) is the largest among the ten polynyas analysed here (see S_p in Table 1). At the time the analysed satellite image was acquired, the area had been subject to prolonged strong WNW winds with speeds exceeding 20 $\mathrm{m{\cdot}s^{-1}}$ for ∼36 hours, and exceeding 30 $\mathrm{m{\cdot}s^{-1}}$ for close to 24 hours (not shown). As the polynya has a relatively regular, symmetric shape, it is useful to examine the wind forcing, and the observed and simulated wave properties on a transect along its central axis (white dashed line in Fig. 1; corresponding maps can be found in Supplementary Figs. S2 and S3). At 21 UTC the AMPS wind (Fig. 6a) along that line oscillates between 30 and 35 $\mathrm{m{\cdot}s^{-1}}$ up to a distance x of ∼50 km from shore, and drops to 25–30 $\mathrm{m{\cdot}s^{-1}}$ only within the last ∼10 km of the polynya. It also gradually changes direction from WNW to WSW, but this change is not fast, in the order of 10° per 30 km. In terms of ice concentration (Fig. 6b), two clearly different regions can be distinguished: for x below and above 40 km. In the first region, the ice concentration varies strongly as the analyzed profile crosses sea-ice and open-water patches, but on average it remains rather low (mean value 0.41). In the second region, it rarely drops below one (mean value 0.98).

As can be seen in Fig. 6c, the no-ice setup of SWAN (S0) significantly overpredicts the peak wave period (by almost 2 s, i.e., close to 30%, in the offshore part of the polynya). It also predicts significant wave heights H_s exceeding 5 m (see Supplementary Fig. S3 for corresponding maps of T_p and H_s). The three 'best' setups identified in section 4.1, S2_f4–S2_f6, produce almost indistinguishable $T_p(x)$ and $H_s(x)$ curves. In agreement with observations, T_p at the downwind end of the polynya exceeds 7 s (corresponding to peak wavelengths of 75–80 m). Notably, H_s reaches maximum at the end of the varying-ice-

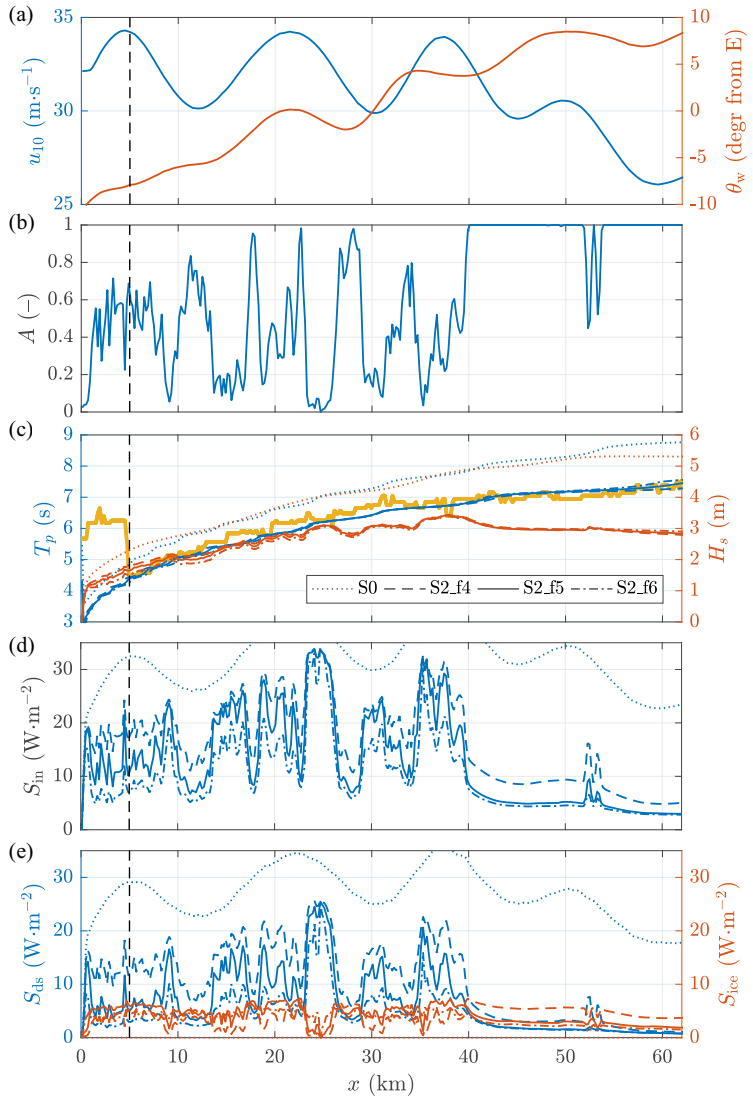

Figure 6. Wind speed u_{10} and direction θ_w (a), ice concentration A (b), significant wave height H_s and peak period T_p (c), wind input S_{in} (d), and dissipation due to wave breaking S_{ds} and in sea ice S_{ice} (e) along the central line of the polynya from 19. Sep. 2019 (see Fig. 1 for transect location). In (c)–(e), the modelling results are shown for four model setups: S0 (dotted lines), S2_f4 (dashed lines), S2_f5 (continuous lines) and S2_f6 (dash-dotted lines); thick yellow line in (c) shows the observed T_p. The black vertical dashed lines at $x = 5$ km mark the boundary of the nearshore region where no reliable wave properties could be determined from the satellite data.

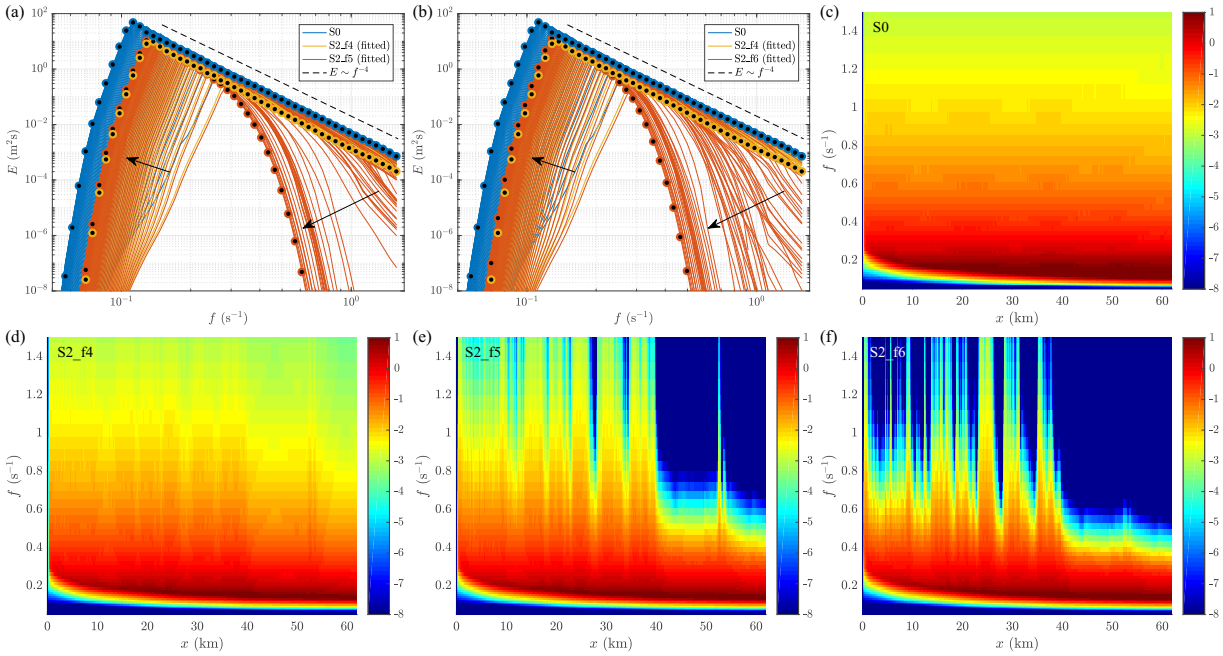

Figure 7. Wave energy spectra $\bar{E}(f)$ along the central line of the polynya from 19. Sep. 2019 (see Fig. 1 for transect location) from four model setups: S0, S2_f4, S2_f5 and S2_f6. In (a,b), every 5th spectrum along the transect is drawn for each setup (S0, S2_f4 and S2_f5 in a, S0, S2_f4 and S2_f6 in b); black arrows mark the direction of increasing x, and the dashed black line has the slope f^{-4}. In (c)–(f), colors show $\log_{10} \bar{E}$ (n m^{2}s) for S0 (c), S2_f4 (d), S2_f5 (e) and S2_f6 (f).

concentration zone, close to $x = 40$ km, and then stays roughly constant at ∼3 m, indicating an approximate balance between wind input and dissipation.

In spite of very similar evolution of the spectral peaks, however, the results of the three setups differ substantially from each other for frequencies above ∼0.4 Hz (Fig. 7). In S2_f4, the tails of the spectra remain very close those in the open-water case S0, even at the downwind end of the polynya. That is, $E \sim f^{-4}$ in the tail (Fig. 7a). In open water it is a signature of the balance between wind input and whitecapping dissipation (red and yellow curves in Fig. 8a–e; see also Fig. 6d,e). Indeed, in S2_f4 $\tilde{S}_{\text{in}}$ and S_{ds} dominate in the spectral tail wherever the ice concentration is relatively low (Fig. 8h). At higher A, $\tilde{S}_{\text{ice}}$ is comparable to S_{ds} (Fig. 8f,g) or even higher (Fig. 8i,j), but the frequency dependence of both source terms is the same – in terms of their mathematical form they are interchangeable. In S2_f5 and S2_f6, to the contrary, ice-induced dissipation of the high-frequency waves is strong enough so that they are almost entirely removed from the spectra as soon as the ice concentration exceeds ∼0.5. This produces spectral shapes similar to those observed in the MIZ (compare brown curves in Fig. 5a,b with, e.g., Fig. 6 of Rogers et al. (2016) or Fig. 2 of Montiel et al. (2022)). As the waves propagate through the patches of grease ice and open water in the central parts of the polynya, the short waves in the spectral tail disappear and reappear as in Fig. 7e,f – an aspect of the results that qualitatively agrees with what is seen in the WV2 image (Figs. 1 and 2).

The consequences of very strong dissipation of short waves in S2_f5 and, especially, S2_f6 are clearly seen in the plots of source terms in Fig. 8k–u. As the wave energy at frequencies higher than ∼0.4 Hz is zero or close to zero in ice-covered locations, the wind input there is close to zero as well – as are all other source terms. Remarkably, in these

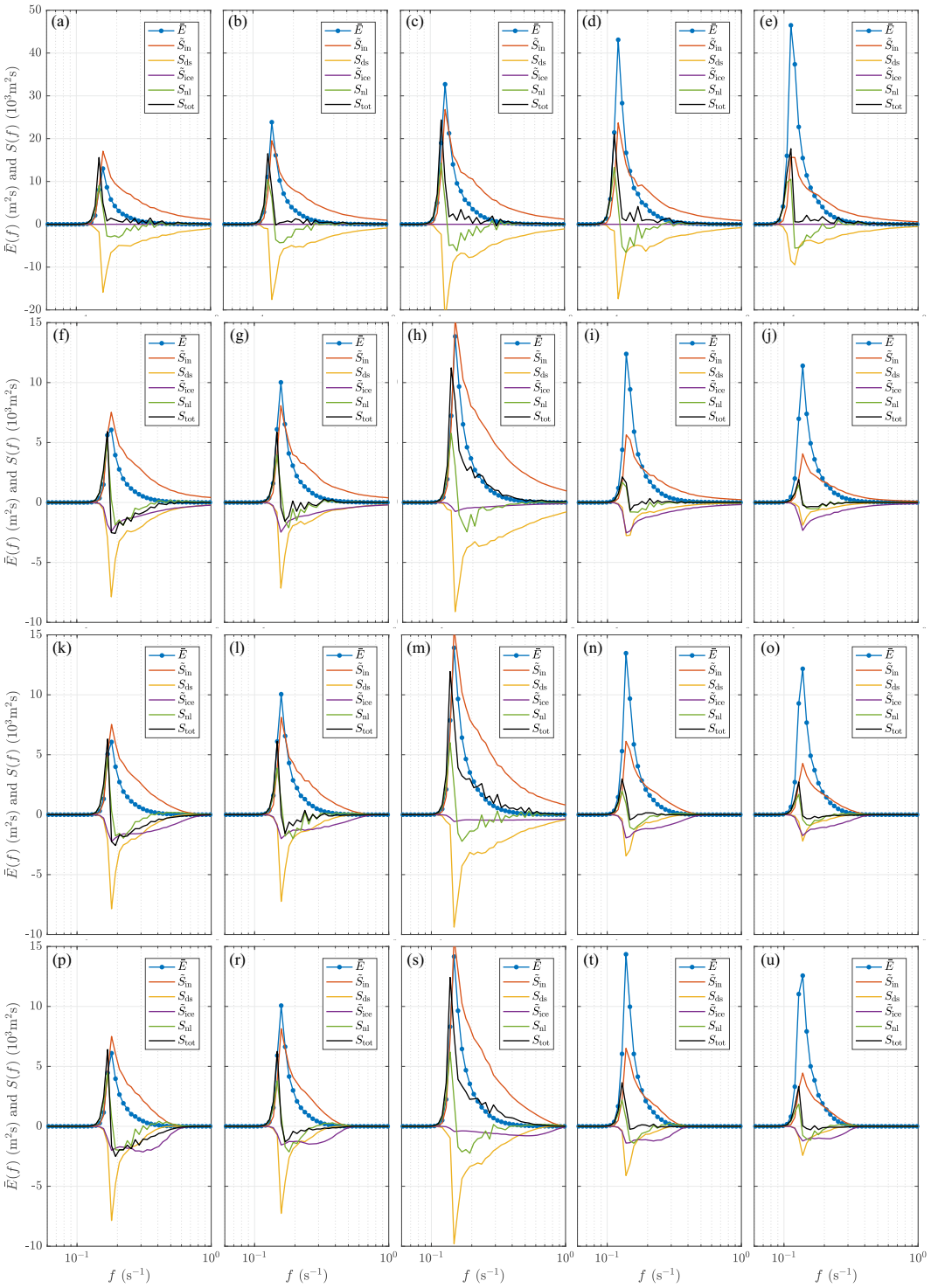

Figure 8. One-dimensional wave energy spectra $\bar{E}(f)$ and source terms at 5 locations along the central line of polynya from 19. Sep. 2019 (white dots in Fig. 1a), from model setups S0 (a–e), S2_f4 (f–j), S2_f5 (k–o) and S2_f6 (p–u). For wind input and sea ice source terms, $\tilde{S}_{\mathrm{in}} = [1 - A + a_{\mathrm{in}}A]S_{\mathrm{in}}$ and $\tilde{S}_{\mathrm{ice}} = AS_{\mathrm{ice}}$ are shown (see equation 1). The black lines show S_{tot}, the sum of all source terms. Note different y-axis scales in (a–e) and (f–u). The ice concentration A at points 1–5 equals 0.72, 0.85, 0.29, 1.00 and 1.00, respectively.

areas the dissipation in sea ice is particularly strong in the range 0.2–0.4 Hz, i.e., just below the no-energy range. If the ice concentration is not too high (Fig. 8k,l,p,r), this energy sink is strengthened by whitecapping, leading to a negative overall energy balance in spite of energy input from wind and, to a lesser extent, from quadruplets. At ice concentration close to 1 (Fig. 8n,o,t,u), the role of whitecapping and quadruplets becomes less significant, and the first-order energy balance is between wind input and ice dissipation. As a net effect, the energy spectra evolve towards narrow, swell-like shapes (see maps of directional spreading in Supplementary Fig. S3).

4.3 Wave breaking

The total surface area of breaking waves estimated from the WV2 data covers 1.08% of the whole area of the analyzed image. Their spatial distribution is inversely correlated with sea ice concentration (Fig. 9a). Considering the whole area of the WV2 image, the contribution of breaking waves to the open-water surface is 1.5%, more than twice as much as in the ice-covered areas, where it is 0.6%. Locally, however, this difference depends on the spatial pattern of frazil streaks – which can bee seen when the two subsets of the WV2 area are analyzed separately (Fig. 10).

Over much of the lower part of the WV2 image (subset 2), the average ice concentration calculated in vertical sections is relatively low and remains between 0.2 and 0.4 with no visible spatial trend (Fig.10). This subset shows narrow streaks of frazil ice that only begin to increase in width and merge near the center of the image and gradually form a more compact ice cover. Under these conditions, the average whitecap fraction W_X changes similarly in open water and in ice, with W_X reaching a maximum at the distance of about 14–16 km from the ice sheet. In this area, the difference between W_X in water and ice remains roughly constant. Only when the average ice concentration increases to about 0.5, at the distance of 21.5 km from shore, a rapid decrease of W_X in streaks and a corresponding increase in open water is observed, producing an order-of-magnitude difference between the W_X in open-water and ice-covered areas.

In the upper part of the image (subset 1), the variability of whitecap fraction in open water are similar (Fig. 10), with a maximum at an approximately the same distance from shore. However, the difference between W_X in open water and ice in subset 1 is generally larger than in subset 2, which can be at least partly explained by the presence of the very wide and long (width ∼500 m) 'mega-streak' – a dominating feature in subset 1. As can be seen i Fig. 9a, it contains almost no whitecaps, contributing to reduced W_X values.

The satellite-based wave breaking patterns cannot be directly compared with modelling results, because spectral wave models do not produce whitecap fraction as output. Therefore, a relationship between W and energy dissipation rate S_{wc} is necessary. To this end, we use formulae derived by Anguelova and Hwang (2016). Assuming that the water is deep, we have:

$$W = c_{\mathrm{W}} \omega_p^4 S_{\mathrm{wc}}, \tag{8}$$

where $\omega_p = 2\pi/T_p$ denotes the peak wave frequency and the coefficient c_{W} is a combination of several empirical constants: $c_{\mathrm{W}} = t_b[4b\rho_w g^3 \log(c_{\max}/c_{\min})\alpha_c^4]^{-1}$. Their values vary strongly between different field and laboratory experiments. Here, without any tuning, we adopt the values from Anguelova and Hwang (2016) for three out of the four coefficients: the bubble persistence time $t_b = 2$ s, the breaking strength parameter $b = 0.013$, and the ratio of maximum to minimum breaker speed $c_{\max}/c_{\min} = 10$. The fourth one, $\alpha_c \in (0, 1)$, denotes the ratio of the threshold breaker speed to the peak wave phase speed. In Anguelova and Hwang (2016), $\alpha_c = 0.3$ is used based on the average from experiments analyzed in Gemmrich et al. (2008). Here, we instead use the modal value of the α_c distribution from the case in Gemmrich et al. (2008) with the highest u_*/c ratio, as it represents a situation closest to the one analyzed here. Thus, we set $\alpha_c = 0.35$.

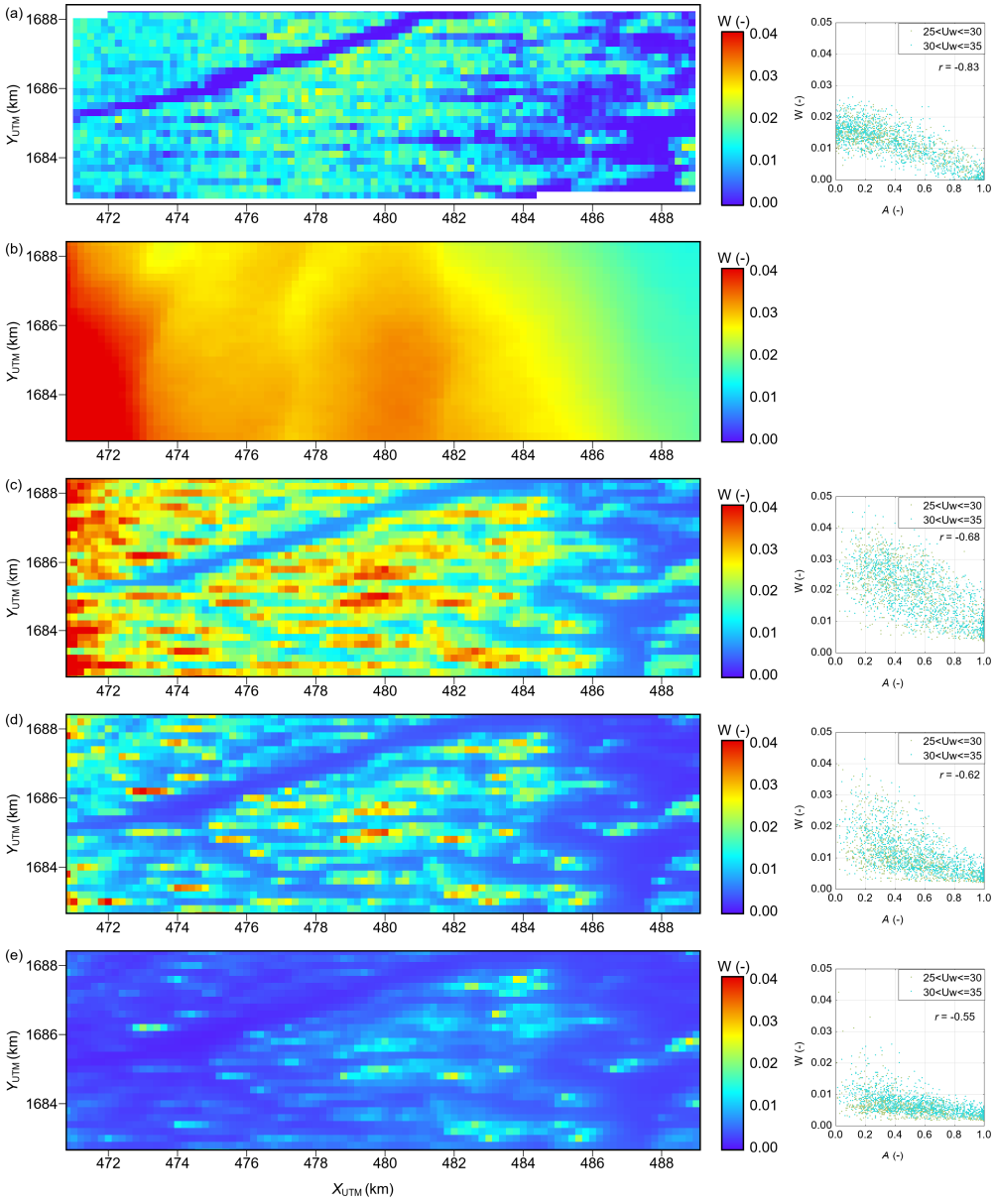

Figure 9. Observed and modelled wave breaking patterns in the area covered by the WV2 image (orange rectangle in Fig. 1). The left panels show maps of whitecap fraction W from the WV2 image (a) and from SWAN simulations with model setup S0 (b), S2_f4 (c), S2_f5 (d) and S2_f6 (e). Right panels show scatterplots of W against ice concentration A for wind speeds below and above 30 m·s^{-1} (green and blue dots).

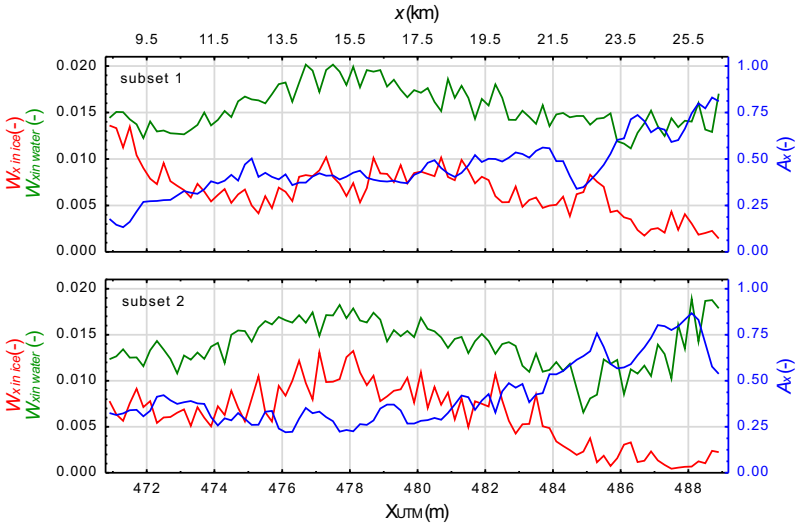

Figure 10. Average ice concentration A_X (right axes) and whitecap fraction W_X computed separately over ice-covered and ice-free regions (left axes) of subsets 1 and 2 of the analyzed WV2 image. X_{UTM} and x denote the UTM coordinates and the distance from the ice sheet, respectively.

The resulting maps of W in the WV2 region from model setups S0, S2_f4, S2_f5 and S2_f6 are shown in Fig. 9b–e. Not surprisingly, the results of the no-ice setup S0 are completely different from satellite observations. However, the remaining three setups produce spatial patterns which are very similar to the observed one – and, at a general level, very similar to each other (this is also true for the whole polynya; see Supplementary Figs. S4 and S5). The best agreement is obtained for S2_f5, which also produces very similar range of values, generally with $W < 0.03$. In S2_f6, wave breaking is very weak, mostly with $W < 0.01$ and with only isolated hotspots of whitecap fractions reaching 0.02. In S2_f4, to the contrary, values exceeding 0.03 are not rare, especially in the leftmost part of the region (a feature absent in satellite-derived data).

It is noteworthy that that the spatial patterns of W and S_{ds} are markedly different (Supplementary Fig. S5) due to the strong wave-frequency dependence of W in equation (8). For the same whitecap fraction W, energy dissipation is lower in long waves than in short waves, and *vice versa*, the same energy dissipation is associated with higher values of W when the waves are shorter. This is responsible for the clearly visible fetch dependence of W in our simulations: the largest values of W can be found nearshore (in all model versions, including S0), when they exceed 0.1. In the case of S_{ds}, it is predominantly influenced by wind speed u_{10} and ice concentration A (Supplementary Figs. S6 and S7). Indeed, as Supplementary Fig. S7 shows for the example of setup S2_f5, $S_{\mathrm{ds}}(u_{10}, A)$ can be easily fit to the data, with the dependence on wind speed being $S_{\mathrm{ds}} \sim u_{10}^{2.88}$, which is very close to the relationship $S_{\mathrm{ds}} \sim u_{10}^{3}$ reported in the literature (Anguelova & Hwang, 2016).

4.4 Global source terms statistics

Although the differences between setups S2_f4–S2_f6 manifest themselves mainly in the tails of the spectra, their effects are clearly visible in spectrally integrated source terms as well (see Fig. 6d,e and maps in Supplementary Fig. S4). The overall spatial patterns remain similar, as they are dictated by the variability of ice concentration, but the amplitude of all source terms varies strongly between setups. Consequently, the total (polynya-

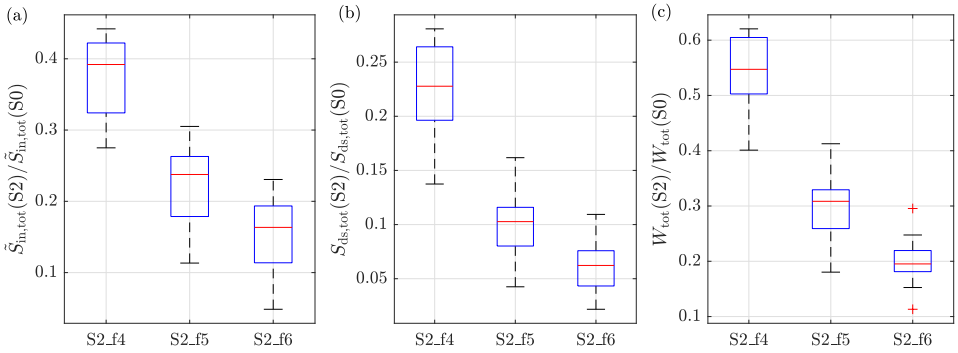

Figure 11. Box plots showing statistics of the ratios $\tilde{S}_{\mathrm{in,tot}}(\mathrm{S2})/\tilde{S}_{\mathrm{in,tot}}(\mathrm{S0})$ (a), $S_{\mathrm{ds,tot}}(\mathrm{S2})/S_{\mathrm{ds,tot}}(\mathrm{S0})$ (b) and $W_{\mathrm{tot}}(\mathrm{S2})/W_{\mathrm{tot}}(\mathrm{S0})$ (c) for the three model versions S2_f4, S2_f5 and S2_f6 and for the ten polynyas analyzed. Red lines show the median values and blue boxes mark the interquartile range.

integrated) energy input from wind, $\tilde{S}_{\mathrm{in,tot}}$, as well as dissipation within sea ice $\tilde{S}_{\mathrm{ice,tot}}$ and due to whitecapping $S_{\mathrm{ds,tot}}$ (with the associated W_{tot}), exhibit very large differences between the ice-free and ice-influenced model versions, hinting at the crucial role of sea ice in modifying polynyas' ocean–atmosphere interactions.

The box plots in Fig. 11 show statistics of the ratios of those global variables in ice-influenced and ice-free model runs, for the ten polynyas analyzed. Although some variability between the ten cases is present, the results are fairly robust (notably, there is no significant correlation between the analyzed ratios and polynya size). Considering that, based on the analysis so far, model settings S2_f5 and S2_f6 best describe available observations, it is save to conclude that the polynya-wide wind input is typically reduced to below 25% of that over open water, the energy dissipation due to whitecapping is reduced to below 10%, and the corresponding coverage of sea surface by whitecaps is reduced to below 30%. These (conservative) estimates decrease with increasing exponent n in the S_{ice} source term. Consequences of the lowered wind input and whitecapping are briefly discussed in the next section.

5 Discussion and conclusions

This study has shown that wind waves in coastal polynyas with frazil streaks are significantly modified by sea ice – and that the role of ice is much more complex than simply dissipating wave energy through viscous processes in a spectral-component-by-component manner. Rather, the net effect of sea ice is a combined result of dissipation, reduced wind input, reduced whitecapping, and modified nonlinear energy transfer within energy spectra. The 'patchiness' of the grease ice cover, typical of polynyas, and the associated alternating removal and re-generation of short waves in the tail of the spectrum play here a particular role. Regarding the four relevant source terms in the wave energy balance equation, the main conclusions of this study are:

- Contrary to the common 'binary' treatment of S_{in} in waves-in-ice modelling (e.g., Li et al., 2015; Cheng et al., 2017; Rogers et al., 2016, 2021), wind input over grease ice is neither equal to that over open water ($a_{\mathrm{in}} = 1$) nor zero ($a_{\mathrm{in}} = 0$). Under conditions of strongly forced waves analyzed here, a constant value of the wind reduction factor $a_{\mathrm{in}} = 0.56$ has been determined based on theoretical arguments and led to a satisfactory model performance. However, as detailed in section 3.2, a_{in} is in fact a function of wind speed and wave frequency. Using a simple param-

706 eterization with constant a_{in} seems reasonable considering very limited observa-
707 tional data on wave growth in ice covered waters, but the analysis in this study
708 provides a general framework for more complex formulations in the future, appli-
709 cable over a wider range of wave ages and frequencies. Regarding the largely un-
710 known variability of the surface drag coefficient C_{Dn} over grease ice in presence
711 of waves, a promising direction of further research might be analogous to param-
712 eterizations of surface drag used in modelling of oil spills, in which the net rough-
713 ness length is computed as a weighted sum of three components, associated with
714 an aerodynamically smooth surface, long waves and short waves, respectively, and
715 the weight of the last component is different over oil and water, reflecting very strong
716 attenuation of short waves in oil-covered regions (Bourassa et al., 1999; Zheng et
717 al., 2013; Blair et al., 2023).
718 • Whitecapping is strongly reduced in regions where frazil streaks are present – not
719 only within streaks themselves, but also in open-water areas between them – con-
720 firming existing qualitative observations from TNBP (Guest, 2021a, 2021b; Ack-
721 ley et al., 2022). Crucially, in the model this effect is obtained without any mod-
722 ifications to the formulation of the S_{ds} term. Rather, reduced whitecapping is a
723 consequence of reduced wave steepness, which in turn results from reduced wind
724 input and from dissipation in sea ice. This does not mean, however, that the open-
725 water formulations of S_{ds} used in the present spectral wave models are fully ad-
726 equate for grease ice regions. It seems likely that the critical steepness used to com-
727 pute S_{wc} in equation (3) is slightly higher in water covered with grease ice than
728 in open water. Moreover, at the same sea surface area fraction covered with break-
729 ers in open water and in grease ice, the amount of dissipated wave energy might
730 be different due to suppressed turbulence and air bubble formation in the latter
731 case.
732 • As long as the developing ice cover is thin and the open-water dispersion relation
733 holds, the quadruplet wave–wave interactions remain unaffected and can be com-
734 puted in the same way as in open water. However, in combination with strong ice-
735 related dissipation in the high-frequency part of the spectrum, their role in regions
736 covered with frazil streaks becomes particularly important. In our simulations, there
737 were substantial differences between the results obtained with DIA and with the
738 quasi-exact method. When using DIA, the very strong positive bias of the wave
739 periods could not be reduced by any reasonable combination of adjustable coef-
740 ficients. With the quasi-exact method, the bias was much smaller and the model
741 calibration unproblematic. Obviously, considering the fact that the computational
742 costs of computing quadruplets in an exact way are over 10^3 times higher than
743 those of DIA, our finding cannot be treated as a recommendation for waves-in-
744 ice modelling, especially in operational or climate applications. However, one should
745 be aware of biases and uncertainties associated with the usage of DIA, and of the
746 danger related to the interpretation of the results of DIA-based models, in which
747 S_{ice} and possibly other source terms must compensate DIA-related biases.
748 • We did not find any evidence of the change of slope n of the sea ice source term
749 with wave frequency. The most straightforward interpretation is that a single phys-
750 ical mechanism is responsible for energy dissipation in the analyzed case, with vis-
751 cous or viscoelastic dissipation the most likely candidates. Crucially, although with
752 the observational data at our disposal we were not able to determine the value of
753 n, we show that $n > 4$ is necessary for a sufficiently strong attenuation in the
754 tail of the spectrum, i.e., for preventing the slope in the tail from reaching the $E \sim$
755 f^{-4} shape, typical for open water. Very importantly, this finding does not con-
756 tradict observations of $n < 4$ in earlier studies (Meylan et al., 2018, and refer-
757 ences there), where it refers to the apparent attenuation from pairs of measured
758 spectra.
759 • Considering the previous conclusion together with the comparison between the satellite-
760 derived and modelled wave breaking patterns, $n = 5$ seems to produce the best

results – but this should be treated as an indication rather than a firm conclusion (and, obviously, n does not have to be a natural number).

- On average, the presence of frazil and grease ice in the analyzed polynyas leads to a reduction of the total wind input to less than 25% of that over open water, and to the reduction of whitecapping dissipation to less than 10%, with the corresponding reduction of the surface area fraction covered with whitecaps to below 30%. Exact values of those ratios depend on the value of n in the S_{ice} term and thus on the intensity of sea ice dissipation.

Some of the above conclusions are specific for polynya conditions. As noted several times throughout this paper, waves in the MIZ typically have lower frequency, are weakly forced by wind, and propagate through a wider variety of ice types. Nevertheless, at several locations where wave–ice interactions have been studied, the conditions are in between those of an 'ideal' MIZ and of a coastal polynya. The Beaufort Sea in the summer and autumn is a good example (Rogers et al., 2016; Smith & Thomson, 2016): the wind fetch is relatively short, frequent low pressure systems are associated with high wind speeds, and a typical ice type is a thin frazil-pancake mixture. Therefore, a proper treatment of the S_{in} and, close to the ice edge, S_{ds} terms is important for reliable spectral modelling, and the present study provides important clues to the formulation of those terms. On the other hand, some of the assumptions made here might be unsuitable for the MIZ. The contribution of nonbreaking-waves dissipation S_{nbr} to the total S_{ds} is just one example – it is negligible in a coastal polynya, where whitecapping dominates over other dissipation mechanisms ($f_{\mathrm{br}} \simeq 1$ in equation (2)), but the opposite might be true for the MIZ, where the waves do not break, but turbulent dissipation in the under-ice boundary layer (Voermans et al., 2019; Herman, 2021) dominates the S_{ds} term.

Our study provides also a very good example of limitations for model development caused by the lack of sufficient observational data. Performing wave-in-ice measurements in the MIZ is very challenging. In coastal polynyas, it is even more difficult due to, first, extreme weather conditions (very high wind speeds, very low air temperatures), and second, short wavelengths, requiring higher spatial (in the case of satellite and airborne imagery) and temporal (in the case of wave buoys and other in situ sensors) resolution. In the TNBP and other coastal polynyas, peak wavelengths only rarely exceed 80–90 m and are lower than that over most of the polynya area. Thus, the usage of many popular synthetic aperture radar (SAR) data sources to retrieve wave energy spectra (e.g., Stopa, Ardhuin, et al., 2018; Wadhams et al., 2018) becomes problematic, as their resolution is comparable with wavelength. Even if peak wavelengths can be determined with sufficient accuracy, estimation of the spectral tails is unreliable. This study has shown that, although spatial variability of peak periods (and other wave properties at the spectral peak) provides a very valuable information on the underlying physics, there are limitations to this approach and the knowledge of spectral tails is crucial for making inferences about the frequency dependence of physical processes shaping the energy spectra. Notably, collecting *in situ* wave data from polynyas is challenging as well, e.g., in the case of wave buoys a serious problem is contamination of measured velocities from heavy buoy tilting, heaving, as well as very fast drift (exceeding 1 m/s; Ackley et al., 2022). In general, the question facing both observations and modelling is whether and how data analysis methods, (semi)empirical parameterizations etc., formulated and tested under 'typical' conditions, can be transferred to the extreme conditions of polynyas without violating their underlying assumptions. In particular, in the case of spectral wave modelling, it is an open issue how expressions (4)–(6) can be made more adequate for polynya events. A related challenge is reconciling information from observations and models. In this study, we obtained two different measures of wave breaking in the analyzed area – one in the form of whitecap fraction W (from a visible satellite image), and one in the form of energy dissipated per unit surface area S_{wc} (from a spectral wave model). The $W(S_{\mathrm{wc}})$ formula from Anguelova and Hwang (2016) with default coefficients happens to produce model-based values of W very close to those determined from satellite data. However,

this and similar relationships suffer from the same problems as the ones mentioned above: the wind speeds in this study are outside the range of observations used to formulate them.

Finally, it is worth commenting on the consequences of the significantly reduced wind input and whitecapping dissipation due to the presence of sea ice in polynyas. One of them are lower rates of sea spray production (due to both lower whitecap fractions W and, likely, less intense bubble and spray generation in breaking waves when grease ice is present), which has been shown to contribute large part of the total ocean–atmosphere turbulent heat flux at high wind speeds. Thus, suppressed whitecapping should lead to significantly lower ocean mixed layer heat loss and, consequently, lower sea ice production rates.

Data Availability Statement

The code of SWAN model is freely available at `http://www.swan.tudelft.nl`. Input files necessary to reproduce our simulations, together with modeling results, can be found at `https://zenodo.org/record/8308164` (Herman & Bradtke, 2023).

Acknowledgments

This work has been financed by Polish National Science Centre projects no. 2018/31/B/ST10/00195 ("Observations and modeling of sea ice interactions with the atmospheric and oceanic boundary layers") and 2022/47/B/ST10/01129 ("Sea ice, waves and turbulence – from laboratory scale to improved large-scale modelling"), and by the University of Gdansk, Laboratory of Physical Oceanography, DS 531-OA02-D425-23. All calculations were carried out at the Academic Computer Centre (TASK) in Gdańsk, Poland.

References

Ackley, S., Smith, M., Guest, P., Herman, A., & Shen, H. (2022). Winds, waves and ice formation in a coastal polynya. In *Proc. 26th iahr international symposium on ice.* IAHR. (Montréal, Canada, 19–23 June 2022)

Alberello, A., Bennetts, L., Onorato, M., Vichi, M., MacHutchon, K., Eayrs, C., ... Toffoli, A. (2022). Three-dimensional imaging of waves and floes in the marginal ice zone during a cyclone. *Nature Comm.*, *13*, 4590. doi: 10.1038/s41467-022-32036-2

Alpers, W., & Hühnerfuss, H. (1989). The damping of ocean waves by surface films: a new look at an old problem. *J. Geophys. Res.*, *94*, 6251–6265. doi: 10.1029/JC094iC05p06251

Alves, J., & Banner, M. (2003). Performance of a saturation-based dissipation-rate source term in modelling the fetch-limited evolution of wind waves. *J. Phys. Oceanogr.*, *33*, 1274–1298. doi: 10.1175/1520-0485(2003)033⟨1274:POASDS⟩2.0.CO;2

Anguelova, M., & Hwang, P. (2016). Using energy dissipation rate to obtain active whitecap fraction. *J. Phys. Oceanogr.*, *46*, 461–481. doi: 10.1175/JPO-D-15-0069.1

Benetazzo, A., Cavaleri, L., Ma, H., Jiang, S., Bergamasco, F., Jiang, W., ... Qiao, F. (2019). Analysis of the effect of fish oil on wind waves and implications for air–water interaction studies. *Ocean Sci.*, *15*, 725–743. doi: 10.5194/os-15-725-2019

Blair, D., Zheng, Y., & Bourassa, M. (2023). The effect of surface oil on ocean wind stress. *Earth*, *4*, 345–364. doi: 10.3390/earth4020019

Booij, N., Ris, R., & Holthuijsen, L. (1999). A third-generation wave model for coastal regions: 1. Model description and validation. *J. Geophys. Res.*, *104C*, 7649–7666. doi: 10.1029/98JC02622

Bourassa, M., Vincent, D., & Wood, W. (1999). A flux parameterization including the effects of capillary waves and sea state. *J. Atmos. Sci.*, *56*, 1123–1139. doi: 10.1175/1520-0469(1999)056⟨1123:AFPITE⟩2.0.CO;2

Boutin, G., Lique, C., Ardhuin, F., Rousset, C., Talandier, C., Accensi, M., & Girard-Ardhuin, F. (2020). Towards a coupled model to investigate wave–sea ice interactions in the Arctic marginal ice zone. *The Cryosphere*, *14*, 709–735. doi: 10.5194/tc-14-709-2020

Bradtke, K., & Herman, A. (2023). Spatial characteristics of frazil streaks in the Terra Nova Bay polynya from high-resolution visible satellite imagery. *The Cryosphere*, *17*, 2073—2094. doi: 10.5194/tc-17-2073-2023

Cheng, S., Rogers, W., Thomson, J., Smith, M., Doble, M., Wadhams, P., ... Shen, H. (2017). Calibrating a viscoelastic sea ice model for wave propagation in the Arctic fall marginal ice zone. *J. Geophys. Res.*, *122*, 8740–8793. doi: 10.1002/2017JC013275

Ciappa, A., & Pietranera, L. (2013). High resolution observations of the Terra Nova Bay polynya using COSMO-SkyMed X-SAR and other satellite imagery. *J. Marine Systems*, *113–114*, 42–51. doi: 10.1016/j.jmarsys.2012.12.004

Collins, C., & Rogers, W. (2017). *A source term for wave attenuation by sea ice in WAVEWATCH III: IC4* (Tech. Rep. Nos. NRL/MR/7320–17-9726). Naval Research Laboratory. (25 pp.)

Collins, C., Rogers, W., & Lund, B. (2017). An investigation into the dispersion of ocean surface waves in sea ice. *Ocean Dynamics*, *67*, 263–280. doi: 10.1007/s10236-016-1021-4

Cox, C., Zhang, X., & Duda, T. (2017). Suppressing breakers with polar oil films: Using an epic sea rescue to model wave energy budgets. *Geophys. Res. Lett.*, *44*, 1414–1421. doi: 110.1002/2016GL071505

Deike, L., Berhanu, M., & Falcon, E. (2017). Experimental observation of hydroelastic three-wave interactions. *Phys. Rev. Fluids*, *2*, 064803. doi: 10.1103/PhysRevFluids.2.064803

Dumont, D. (2022). Marginal ice zone dynamics: history, definitions and research perspectives. *Phil. Trans. Royal Soc. A*, *380*, 20210253. doi: 10.1098/rsta.2021.0253

Eicken, H., & Lange, M. (1989). Development and properties of sea ice in the coastal regime of the Southeastern Weddell Sea. *J. Geophys. Res.*, *94*, 8193-8206. doi: 10.1029/JC094iC06p08193

Garbrecht, T., Lüpkes, C., Hartmann, J., & Wolff, M. (2002). Atmospheric drag coefficients over sea ice – validation of a parameterisation concept. *Tellus*, *54A*, 205–219.

Gemmrich, J., Banner, M., & Garrett, C. (2008). Spectrally resolved energy dissipation rate and momentum flux of breaking waves. *J. Phys. Oceanogr.*, *38*, 1296–1312. doi: 10.1175/2007JPO3762.1

Guest, P. (2021a). Inside katabatic winds over the Terra Nova Bay Polynya: 1. Atmospheric jet and surface conditions. *J. Geophys. Res.: Atmospheres*, *126*, e2021JD034902. doi: 10.1029/2021JD034902

Guest, P. (2021b). Inside katabatic winds over the Terra Nova Bay Polynya: 2. Dynamic and thermodynamic analyses. *J. Geophys. Res.: Atmospheres*, *126*, e2021JD034904. doi: 10.1029/2021JD034904

Hasselmann, S., Hasselmann, K., Allender, J., & Barnett, T. (1985). Computations and parameterizations of the nonlinear energy transfer in a gravity wave spectrum. Part II: Parameterizations of the nonlinear transfer for application in wave models. *J. Phys. Oceanogr.*, *15*, 1378–1391. doi: 10.1175/1520-0485(1985)015⟨1378:CAPOTN⟩2.0.CO;2

Herman, A. (2021). Spectral wave energy dissipation due to under-ice turbulence. *J. Phys. Oceanogr.*, *51*, 1177–1186. doi: 10.1175/JPO-D-20-0171.1

Herman, A., & Bradtke, K. (2023). *SWAN wave model simulations of the Terra*

Nova Bay Polynya. Data set, Zenodo. doi: 10.5281/zenodo.8308164

Herman, A., Dojczman, M., & Świszcz, K. (2020). High-resolution simulations of interactions between surface ocean dynamics and frazil ice. *The Cryosphere*, *14*, 3707–3729. doi: 10.5194/tc-14-3707-2020

Hollands, T., & Dierking, W. (2016). Dynamics of the Terra Nova Bay Polynya: The potential of multi-sensor satellite observations. *Remote Sens. Environ.*, *187*, 30–48. doi: 10.1016/j.rse.2016.10.003

Holthuijsen, L. (2007). *Waves in oceanic and coastal waters.* Cambridge Univ. Press. (387 pp.)

Janssen, P., & Bidlot, J.-R. (2023). Wind–wave interaction for strong winds. *J. Phys. Oceanogr.*, *53*, 779–804. doi: 10.1175/JPO-D-21-0293.1

Janssen, P., Lionello, P., & Zambresky, L. (1989). On the interaction of wind and waves. *Phil. Trans. Royal Soc. A*, *329*, 289–301. doi: 10.1098/rsta.1989.0077

Kohout, A., Smith, M., Roach, L., Williams, G., Montiel, F., & Williams, M. (2020). Observations of exponential wave attenuation in Antarctic sea ice during the PIPERS campaign. *Ann. Glaciology*, *61*, 196–209. doi: 10.1017/aog.2020.36

Komen, G., Hasselmann, S., & Hasselmann, K. (1984). On the existence of a fully developed wind-sea spectrum. *J. Phys. Oceanogr.*, *14*, 1271–1285. doi: 10.1175/1520-0485(1984)014⟨1271:OTEOAF⟩2.0.CO;2

Li, J., Kohout, A., & Shen, H. (2015). Comparison of wave propagation through ice covers in calm and storm conditions. *Geophys. Res. Lett.*, *42*, 5935–5941. doi: 10.1002/2015GL064715

Liu, Q., Rogers, W., Babanin, A., Li, J., & Guan, C. (2020). Spectral modeling of ice-induced wave decay. *J. Phys. Oceanogr.*, *50*, 1583–1604. doi: 10.1175/JPO-D-19-0187.1

Lüpkes, C., & Birnbaum, G. (2005). Surface drag in the Arctic marginal sea-ize zone: Comparison of different parameterisation concepts. *Bound. Layer Meteorol.*, *117*, 179–211.

Lüpkes, C., Gryanik, V., Hartmann, J., & Andreas, E. (2012). A parametrization, based on sea ice morphology, of the neutral atmospheric drag coefficients for weather prediction and climate models. *J. Geophys. Res.*, *117*, D13112. doi: 10.1029/2012JD017630

Mchedlishvili, A., Lüpkes, C., Petty, A., Tsamados, M., & Spreen, G. (2023). New estimates of the pan-Arctic sea ice-atmosphere neutral drag coefficients from ICESat-2 elevation data. *EGUsphere*, *preprint*. doi: 10.5194/egusphere-2023-187

Meylan, M., Bennetts, L., & Kohout, A. (2014). In situ measurements and analysis of ocean waves in the Antarctic marginal ice zone. *Geophys. Res. Lett.*, *41*, 5046–5051. doi: 10.1002/2014GL060809

Meylan, M., Bennetts, L., Mosig, J., Rogers, W., Doble, M., & Peter, M. (2018). Dispersion relations, power laws, and energy loss for waves in the marginal ice zone. *J. Geophys. Res.*, *123*, 3322–3335. doi: 10.1002/2018JC013776

Montiel, F., Kohout, A., & Roach, L. (2022). Physical drivers of ocean wave attenuation in the marginal ice zone. *J. Phys. Oceanogr.*, *52*, 889–906. doi: 10.1175/JPO-D-21-0240.1

Morales Maqueda, M., Willmott, A., & Biggs, N. (2004). Polynya dynamics: A review of observations and modeling. *Rev. Geophys*, *42*, RG1004. doi: 10.1029/2002RG000116

Nakata, K., Ohshima, K., & Nihashi, S. (2021). Mapping of active frazil for Antarctic coastal polynyas, with an estimation of sea-ice production. *Geophys. Res. Lett.*, *48*, e2020GL091353. doi: 10.1029/2020GL091353

Powers, J., Manning, K., Bromwich, D., Cassano, J., & Cayette, A. (2012). A decade of Antarctic science support through AMPS. *Bull. Am. Meteorol. Soc.*, *93*(11), 1699–1712. doi: 10.1175/BAMS-D-11-00186.1

Roach, L., Bitz, C., Horvat, C., & Dean, S. (2019). Advances in modeling inter-

actions between sea ice and ocean surface waves. *J. Advances Mod. Earth Systems*, *11*, 4167–4181. doi: 10.1029/2019MS001836

Roach, L., Horvat, C., Dean, S., & Bitz, C. (2018). An emergent sea ice floe size distribution in a global coupled ocean–sea ice model. *J. Geophys. Res.*, *123*, 4322–4337. doi: 10.1029/2017JC013692

Rogers, W. (2019). *Implementation of sea ice in the wave model SWAN* (Tech. Rep. Nos. NRL/MR/7322–19-9874). Naval Research Laboratory, USA. (25 pp.)

Rogers, W., Hwang, P., & Wang, D. (2003). Investigation of wave growth and decay in the SWAN model: three regional-scale applications. *J. Phys. Oceanogr.*, *33*, 366–389. doi: 10.1175/1520-0485(2003)033⟨0366:IOWGAD⟩2.0.CO;2

Rogers, W., Meylan, M., & Kohout, A. (2018). *Frequency distribution of dissipation of energy of ocean waves by sea ice using data from Wave Array 3 of the ONR "sea state" field experiment* (Tech. Rep. Nos. NRL/MR/7322–18-9801). Naval Research Laboratory, USA. (32 pp.)

Rogers, W., Meylan, M., & Kohout, A. (2021). Estimates of spectral wave attenuation in Antarctic sea ice, using model/data inversion. *Cold Regions Sci. Tech.*, *182*, 103198. doi: 10.1016/j.coldregions.2020.103198

Rogers, W., Posey, P., Li, L., & Allard, R. (2018). *Forecasting and hindcasting waves in and near the marginal ice zone: wave modeling and the ONR "sea state" field experiment* (Tech. Rep. Nos. NRL/MR/7320–18-9786). Naval Research Laboratory, USA. (183 pp.)

Rogers, W., Thomson, J., Shen, H., Doble, M., Wadhams, P., & Cheng, S. (2016). Dissipation of wind waves by pancake and frazil ice in the autumn Beaufort Sea. *J. Geophys. Res.*, *121*, 7991–8007. doi: 10.1002/2016JC012251

Shen, H. (2022). Wave-in-ice: theoretical bases and field observations. *Phil. Trans. Royal Soc. A*, *380*, 20210254. doi: 10.1098/rsta.2021.0254

Smith, M., & Thomson, J. (2016). Scaling observations of surface waves in the Beaufort Sea. *Elementa*, *4*, 000097. doi: 10.12952/journal.elementa.000097

Smith, M., & Thomson, J. (2019a). Ocean surface turbulence in newly formed marginal ice zones. *J. Geophys. Res.*, *124*, 1382–1398. doi: 10.1029/2018JC014405

Smith, M., & Thomson, J. (2019b). Pancake sea ice kinematics and dynamics using shipboard stereo video. *Annals Glaciology*, *61*, 1–11. doi: 10.1017/aog.2019.35

Squire, V. (2018). A fresh look at how ocean waves and sea ice interact. *Phil. Trans. R. Soc. A*, *376*, 20170342. doi: 10.1098/rsta.2017.0342

Squire, V. (2020). Ocean wave interactions with sea ice: A reappraisal. *Annu. Rev. Fluid Mech.*, *52*, 37–60. doi: 10.1146/annurev-fluid-010719-060301

Stopa, J., Ardhuin, F., Thomson, J., Smith, M., Kohout, A., Doble, M., & Wadhams, P. (2018). Wave attenuation through an Arctic marginal ice zone on 12 October 2015. 1. Measurement of wave spectra and ice features from Sentinel 1A. *J. Geophys. Res.*, *123*. doi: 10.1029/2018JC013791

Stopa, J., Sutherland, P., & Ardhuin, F. (2018). Strong and highly variable push of ocean waves on Southern Ocean sea ice. *Proc. Nat. Acad. Sci.*, *115*, 5861–5865. doi: 10.1073/pnas.1802011115

SWAN Team. (2022). *SWAN Cycle III, version 41.45, Scientific and Technical Documentation* (Tech. Rep.). Delft University of Technology, Faculty of Civil Engineering and Geosciences.

Thompson, L., Smith, M., Thomson, J., Stammerjohn, S., Ackley, S., & Loose, B. (2020). Frazil ice growth and production during katabatic wind events in the Ross Sea, Antarctica. *The Cryosphere*, *14*, 3329–3347. doi: 10.5194/tc-14-3329-2020

Van der Westhuijsen, A., Zijlema, M., & Battjes, J. (2007). Nonlinear saturationbased whitecapping dissipation in SWAN for deep and shallow water. *Coastal Engng*, *54*, 151–170. doi: 10.1016/j.coastaleng.2006.08.006

Van Vledder, G. P. (2006). The WRT method for the computation of non-linear four-wave interactions in discrete spectral wave models. *Coastal Engng*, *53*, 223–242. doi: 10.1016/j.coastaleng.2005.10.011

Voermans, J., Babanin, A., Thomson, J., Smith, M., & Shen, H. (2019). Wave attenuation by sea ice turbulence. *Geophys. Res. Lett.*, *46*, 6796–6803. doi: 10.1029/2019GL082945

Wadhams, P., Aulicino, G., Parmiggiani, F., Persson, P., & Holt, B. (2018). Pancake ice thickness mapping in the Beaufort Sea from wave dispersion observed in SAR imagery. *J. Geophys. Res.*, *123*, 2213–2237. doi: 10.1002/2017JC013003

Yan, L. (1987). *An improved wind input source term for third generation ocean wave modelling* (Tech. Rep. Nos. 87–8). Royal Dutch Meteor. Inst. (20 pp.)

Zhao, X., & Zhang, C. (2020). A theoretical model of wind-wave growth over an ice-covered sea. *Boundary Layer Meteorol.*, *178*, 1–19. doi: 10.1007/s10546-020-00552-7

Zheng, Y., Bourassa, M., & Hughes, P. (2013). Influence of sea surface temperature gradients and surface roughness changes on the motion of surface oil: a simple idealized study. *J. Applied Meteorol. Clim.*, *52*, 1561–1575. doi: 10.1175/JAMC-D-12-0211.1

Zijlema, M., van Veldder, G., & Holthuijsen, L. (2012). Bottom friction and wind drag for wave models. *Coastal Engng*, *65*, 19–26. doi: 10.1016/j.coastaleng.2012.03.002